14

Visualization Systems for Multi-Dimensional Microscopy Images

N.S. White

INTRODUCTION

Rapid developments in biological microscopy have prompted many advances in multi-dimensional imaging. However, three-dimensional (3D) visualization techniques originated largely from applications involving computer-generated models of macroscopic objects. Subsequently, these methods have been adapted for biological visualization of mainly tomographic medical images and data from cut serial sections (e.g., Cookson *et al*., 1989 and review in Cookson, 1994). Most of these algorithms were not devised specifically for microscopy images, and only a few critical assessments have been made of suitable approaches for the most common 3D technique, laser-scanning microscopy (LSM) (Kriete and Pepping, 1992). Ultimately, we must rely on objective visualization of control, calibration, and test specimens in order to determine which visualization algorithms are appropriate for a particular analysis. Hardware developments and advances in software engineering tools have made available many 3D reconstruction systems that can be used to visualize multi-dimensional images. These are available from instrument manufacturers, third party vendors, research academics, and other microscopists. The author has attempted to collate important techniques used in these programs and to highlight particular packages that, not exclusively, illustrate various techniques described throughout the text. A representative collection of established commercial and non-commercial visualization programs available at the time of writing is listed in Table 14.1. For automatic image analysis and measurement, see Chapters 15 and 48, *this volume*.

The information presented in this chapter about the various programs is not the result of exhaustive tests or benchmarks but is merely an overall view of some key issues. The speed of changes and the rapid appearance (and loss) of particular programs and hardware from common use make it necessary to concentrate on important techniques and milestones rather than intricate details of each package.

Multi-dimensional microscopy data can also be obtained from instruments other than LSM configurations, such as non-laser confocal devices and widefield (conventional) systems combined with image restoration. Although the multi-dimensional data from different instruments may have different characteristics, the same basic visualization methods can be used to process the data.

Definitions

A consistent terminology is required to discuss components of any visualization system, maintaining a fundamental separation between (1) raw images and subsequent processed stages, (2) data values and the sampled space over which they extend, and (3) final results and the presentation form of those results. The author prefers the following terminology: Original intensities from the microscope comprise an **image**. Subsequent visualization steps produce a **view**. Intensities in an image or view represent the **data values**, and the sampling space over which they extend constitutes the **dimensions of the data**. Values presented on a screen, hard copy, etc., are **display views**. **Visualization** is the overall process by which a multi-dimensional display view is made from a biological specimen, although we will only be concerned with the software component of this in the present text. **Reconstruction** refers to the piecing together of optical sections into a representation of the specimen object. **Rendering** is a computer graphics term that describes the drawing of reconstructed objects into a display view.

What Is the Microscopist Trying to Achieve?

Human visual perception and cognition are highly adapted to interpret views of large-scale (macroscopic) objects. The human eye captures low numerical aperture (NA) views like photographic images. We get information from such views by calling (largely subconsciously) on *a priori* information about both the object and imaging system. High-NA microscope objectives produce images from which we generate views with properties that we are less equipped to interpret, for example, the apparent transparency of most biological samples. This arises from two main processes: (1) Samples are mostly thin, non-absorbing, and scatter only some of the illuminating light. Reduced out-of-focus blur, together with this real transparency enable the confocal and multi-photon LSMs to probe deep into intact specimens. (2) A high-NA microscope objective collects light from a large solid angle and can see around small opaque structures that would otherwise obscure or shadow details further into the sample. Such intrinsic properties in the resultant images must be sympathetically handled by an appropriate visualization system.

The goal of visualization is the formation of easily interpreted and, sometimes, realistic-looking display views. While pursuing these aims, several conflicts arise: (1) avoiding visualization artifacts from inappropriate *a priori* knowledge, (2) enhancing selected features of interest, and (3) retaining quantitative information. Maintaining these goals ensures that the final view can be used to help obtain unbiased measurements or to draw unambiguous conclusions. **The microscopist must be constantly vigilant to avoid unreasonably distorting the structural (and intensity) information in the original image data by over-zealous use of image processing.**

N.S. White • University of Oxford, Oxford OX1 3RE, United Kingdom

Criteria for Choosing a Visualization System

Assessing any visualization system requires a judgment of (1) features, (2) usability or friendliness, (3) price/performance, (4) suitability of algorithms, (5) integration with existing systems, and (6) validation and documentation of methods or algorithms. The only way to determine ease of use is by testing the system with typical users and representative data. The best demonstration images saved at a facility should never be used to assess a visualization system for purchase! The host institution's user profile will help to formulate more specific questions: What is the purpose of the reconstructed views? What image information can be represented in the display views? How must the image data be organized? Are semi-automated or script-processing (programming) tools available for preprocessing and can the procedures be adequately tested and tracked?

WHY DO WE WANT TO VISUALIZE MULTI-DIMENSIONAL LASER-SCANNING MICROSCOPY DATA?

The principle uses of a visualization package are to generate subregion or composite reconstructions from multi-dimensional images (Fig. 14.1). To collect such views directly from the microscope is a time-consuming and inefficient process.

There are many advantages to interactively viewing multidimensional confocal images away from the microscope:

- Damage to the sample by the illumination is reduced.
- Sample throughput on a heavily used system is improved.
- Optimal equipment for data presentation and analysis can be employed. Serial two-dimensional (2D) orthogonal sections (e.g., *xy*, *xz*, *yz*, *xt*, etc.) must be extracted from a 3D/four-dimensional (4D) image interactively at speeds adequate for smooth animation. An animation of confocal sections corresponds to a digital focal series without contrast-degrading blur. Oblique sections overcome the serial section bias of all confocal instruments and their smooth, interactive animation is desirable.
- Reconstructed views are essential to conveniently display a 3D (Drebin *et al.*, 1988; Robb, 1990) or 4D image (Kriete and Pepping, 1992) on a 2D display device. The reconstructed volume may show features that are not discernible when animating sequential sections (Cookson *et al.*, 1993; Foley *et al.*, 1990). Reconstructions further reduce the orientationally biased view obtained from serial sections alone.
- Multiple views are a useful way of extending the dimensional limitations of the 2D display device. Montages of views make more efficient use of the pixel display area. Animations make effective use of the display bandwidth. Intelligent use of color can further add to our understanding of the information in a display view (e.g., Boyde, 1992; Kriete and Pepping, 1992; Masters, 1992).
- For multiple-channel images, flexibility and interactive control are essential. Multiple channels may require complex color merging and processing in order to independently control the visualization of each component.

Data and Dimensional Reduction

Simplification of a complex multi-dimensional image to a 2D display view implies an important side effect — data and dimensional reduction. If the required information can be retained in a display view, substantial improvements in storage space and image transfer times are possible. This is increasingly important when presentation results must be disseminated via the Internet (now a routine option for medical imaging packages such as those from Cedara and Vital Images Inc.). Data reduction is most obvious in the case of a single (2D) view of a 3D volume or multiple-channel image but is actually more significant when 4D data can be distilled into a series of 2D views (Volocity, Imaris, and Amira, among other packages, can now seamlessly visualize multi-channel 4D images). Significant reduction can also be achieved when a single 3D volume of voxels can be represented by a smaller number of geometric objects. To combine data reduction with quantitative analyses, a precise description of the object extraction algorithm must be recorded along with the view; only then can the user determine the significance of extracted features.

Objective or Subjective Visualization?

The conflict between realistic display and objective reconstruction persists throughout the visualization process. All of the important information must be retained in a well-defined framework, defined by the chosen visualization model or algorithm. Recording of the parameters at every stage in the visualization is essential. This can be consistent with the production of convincing or realistic displays, provided enhancement parameters are clearly described and can be called upon during the interpretation phase. Multidimensional image editing must be faithfully logged in order to relate subregions, even those with expansion or zooming, back to their original context. Object extraction is a one-way operation that discards any original image data that falls outside the segmentation limits. To interpret a reconstruction based on graphically drawn surfaces we will need to refer back to the corresponding image voxels. To do this, we must either (1) superimpose the view on a reconstruction that shows the original voxels, using so-called embedded geometries (e.g., Analyze, Amira, Imaris VolVis and others), or (2) make references back to the original image. Voxel distribution statistics defining the degree to which a particular extracted object fits the image data would be a significant improvement.

Prefiltering

Low-pass or median filtering aids segmentation by reducing noise. Ideally, noise filters should operate over all image dimensions, and not just serially on 2D slices. Imaris, Voxblast, and FiRender/LaserVox, for example, have true 3D filters; the latter are particularly useful as they allow filtering of a subvolume for comparison within the original. Because Nyquist sampling will ideally have been adhered to in the image collection, the ideal preprocessing stage would include a suitable Gaussian filter or (even better) a point-spread function (PSF) deconvolution (Agard *et al.*, 1989). This step can effectively remove noise, that is, frequency components outside the contrast transfer function of the instrument.

Identifying Unknown Structures

The first thing to do with a newly acquired 3D image is a simple reconstruction (usually along the focus or *z*-axis). Even the simplest of visualization modules in 2D packages (such as Metamorph and the basic Scion Image) can rapidly project even modest size data sets. The aim is to get an unbiased impression of the significant structure(s). For the reasons discussed above, the method of

TABLE 14.1. A Representative Collection of Visualization Software Packages Available at the Time of Writing

System	Source	Supplier type	Platforms supported	Price Guide
Amira	TGS Inc. 5330 Carroll Canyon Road, Suite 201, San Diego CA 92121, USA www.amiravis.com	ind	Win, HP SGI, Sun Linux	(B)–(C)
Analyze	Analyze Direct 11425 Strang Line Road, Lenexa, KS 66215, USA www.analyzedirect.com	acad ind	Win Unix/Linux	(B)
3D for LSM & LSM Vis Art	Carl Zeiss Microscopy D07740 Jena, Germany www.zeiss.de/lsm	LSM, wf	Win	(A)–(B)
AutoMontage	Syncroscopy Ltd. Beacon House, Nuffield Road, Cambridge, CB4 1TF, UK www.syncroscopy.com	Ind wf	Win	(A)–(B)
AVS	Advanced Visual Systems Inc. 300 Fifth Avenue, Waltham, MA 02451, USA www.avs.com	ind	DEC, SGI, Sun, Linux	(A)–(B)
Cedara (formerly ISG)	Cedara Software Corp. 6509 Airport Road, Mississauga, Ontario, L4V 1S7, Canada www.cedara.com	med	Win	(B)–(C)
Deltavision & SoftWorx	Applied Precision, LLC 1040 12th Avenue Northwest, Issaquah, Washington 98027, USA www.api.com	wf	Win	(B)
FiRender	Fairfield Imaging Ltd. 1 Orchard Place, Nottingham Business Park, Nottingham, NE8 6PX, UK www.fairimag.co.uk	ind	Win	(B)
Image Pro Plus & 3D Constructor	Media Cybernetics, Inc. 8484 Georgia Avenue, Suite 200, Silver Spring, MD 20910–5611, USA www.mediacy.com	ind	Win	(B)
ImageJ	National Institutes of Health 9000 Rockville Pike, Bethesda, Maryland 20892, USA http://rsb.info.nih.gov/ij	acad	Win, Mac Linux, Unix	(A)–(B)
Imaris	Bitplane AG Badenerstrasse 682, CH-8048 Zurich, Switzerland www.bitplane.com	ind	Win	(A)–(C)
Lasersharp & LaserVox & LaserPix	Bio-Rad Microscience Ltd. Bio-Rad House, Maylands Avenue, Hemel Hempstead, HP2 7TD, UK www.cellscience.bio-rad.com	LSM	Win	(A)–(B)
LCS & LCS-3D	Leica Microsystems AG Ernst-Leitz-Strasse 17-37, Wetzlar, 35578, Germany www.leica-microsystems.com	LSM, wf	Win	(A)–(B)
Metamorph	Universal Imaging Corporation 402 Boot Road, Downingtown, PA 19335, USA www.image1.com	ind	Win	(A)–(B)
Northern Eclipse	Empix Imaging, Inc. 3075 Ridgeway Drive, Unit #13, Mississauga, ON, L5L 5M6, CANADA www.empix.com	ind	Win	(A)–(B)
Stereo Investigator	MicroBrightField, Inc. 185 Allen Brook Lane, Suite 201, Williston, VT 05495, USA www.microbrightfield.com	ind	Win	(A)–(B)
Scion Image	Scion Corp. 82 Worman's Mill Court, Suite H, Frederick, Maryland 21701, USA www.scioncorp.com	ind	Win Mac	(A)
Visilog/Kheops	Noesis 6–8, Rue de la Réunion, ZA Courtabœuf, 91540 Les Ulis Cedex, FR www.noesisvision.com	ind	Win Unix	(A)–(B)
Vitrea2 (formerly VoxelView)	ViTAL Images, Inc. 5850 Opus Parkway, Suite 300, Minnetonka, Minnesota 55343, USA www.vitalimages.com	med	Win SGI	(B)–(C)
Volocity & OpenLab	Improvision Inc 1 Cranberry Hill, Lexington, MA 02421, USA www.improvision.com	ind	Win Mac	(B)–(C)
VolumeJ (plug-in for ImageJ)	Michael Abramoff, MD, PhD University of Iowa Hospitals and Clinics, Iowa, USA http://bij.isi.uu.nl	acad	Win, Mac Linux, Unix	(A)–(B)
VolVis	Visualization Lab Stony Brook University, New York, USA www.cs.sunysb.edu/~vislab	ind	Unix source supplied	(A)

TABLE 14.1. (*Continued*)

System	Source	Supplier type	Platforms supported	Price Guide
VoxBlast	VayTek, Inc.	ind	Win	(A)–(C)
	305 West Lowe Avenue, Suite 109, Fairfield, IA 52556, USA		Mac	
	www.vaytek.com		SGI	
Voxx	Indiana Center for Biological Microscopy	acad	Win	(A)–(B)
	Indiana University Medical Center		Mac	
	www.nephrology.iupui.edu/imaging/voxx		Linux	

Ind = independent supplier (not primarily a microscopy system supplier), acad = system developed in, and supported by, academic institution, LSM = LSM supplier, wf = widefield microscopy system supplier, med = medical imaging supplier. Win = Microsoft Windows, Mac = Apple Macintosh, SGI = Silicon Graphics workstation, HP = Hewlett Packard workstation. Price guide (very approximate, lowest price includes entry level hardware platform): (A) = < $5000, (B) = $5000–$15,000, (C) = > $15,000.

choice is voxel rendering, as it avoids potential artifacts of segmentation at this early stage. This catch-all algorithm could have interactive parameter entry in order to explore the new structure if the processing were fast enough. Contrast control and careful data thresholding (to remove background only) would normally be used with this quick-look approach. More specific voxel segmentation (removing data values outside a given brightness band, intensity gradient, or other parameter range) should be used with caution during the identification of a new structure. Artifactual boundaries (surfaces) or apparently connected structures (e.g., filaments) can always be found with the right segmentation and contrast settings.

In subsequent refinement stages, a case can usually be made for a more specific segmentation model. For example, maximum intensity segmentation can be used to visualize a topological reflection image of a surface. The prerequisites for such a choice can only be confirmed by inspection of the entire image data. Finally, visualization models involving more complex segmentation, absorption and lighting effects, whether artificial or based on *a priori* knowledge, must be introduced in stages after the basic distribution of image intensities has been established (Fig. 14.2).

Computer graphics research is beginning to offer techniques for automated or computer-assisted refinement of the visualization algorithm to automatically tune it for the particular supplied data (He *et al.*, 1996; Marks, 1997; Kindlmann and Durkin, 1998). Some useful user-interface tools, such the Visual Network Editor of AVS, assist in the design stages of more complex multi-step or interactive visualization procedures.

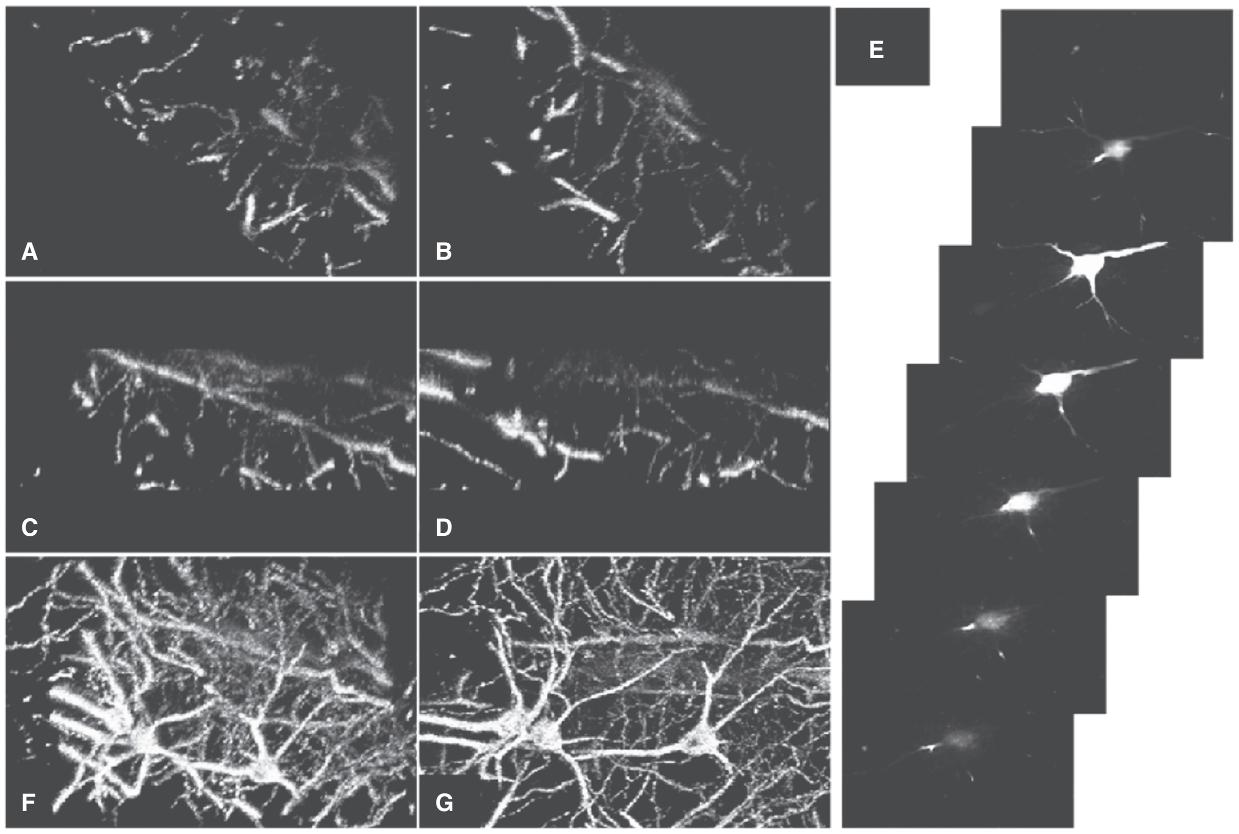

FIGURE 14.1. Viewing multidimensional LSM data. In order to make maximum use of imaging resources, multidimensional CLSM images are routinely viewed away from the microscope. "Thick" 2D oblique sections (A, B) can be extracted at moderate rates by many software packages. 2D orthogonal sections (C–E) can be viewed at video rate. Reconstructed 3D views (F, G) require more extensive processing, now common in all commercial systems. (A–D, F, G) are reflection images of Golgi-stained nerve cells. (E) Multiple *xy* views (e.g., from an animation) of fluorescently stained nerve cells.

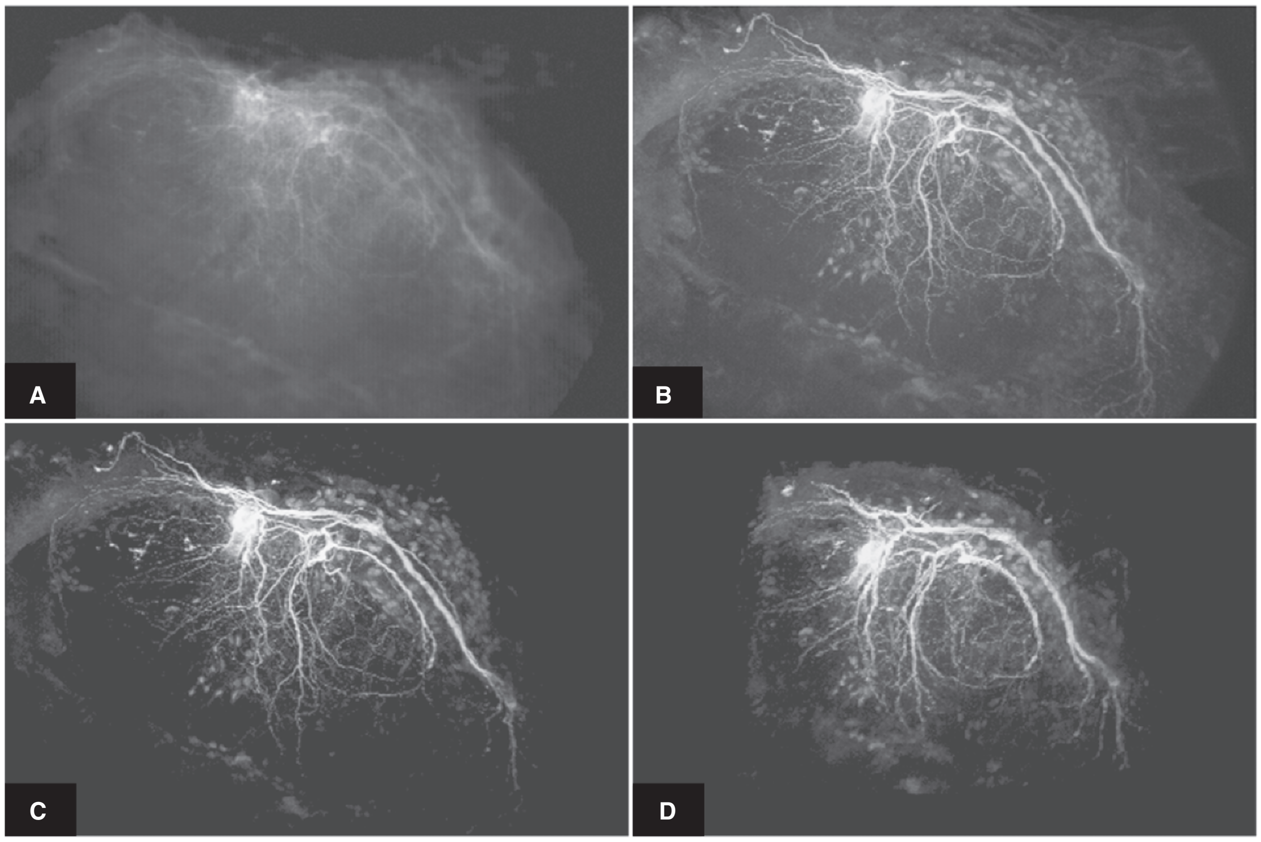

FIGURE 14.2. Identifying unknown structures. It is important to make as few assumptions as possible about the imaged structures during the exploratory phase of 3D visualization. Average (or summation) projection (A), though simple, often gives low-contrast views due to the low weight given to small structures. Maximum brightness (B) gives higher weight to small bright structures but when used in isolation provides no *z*-discrimination. (C) Background thresholding (setting to zero below a base line) is simple, easy to interpret and increases contrast in the view. (D) Re-orientating the 3D volume (even by a few degrees) can show details not seen in a "top down view," and coupled with animation (see text), this is a powerful exploratory visualization tool. (A–C) processed by simple *z*-axis projections, (D) "Maximum intensity" using the Lasersharp software. Lucifer Yellow stained nerve cell supplied by S. Roberts, Zoology Department, Oxford University.

Highlighting Previously Elucidated Structures

Having ascertained the importance of a particular feature, the next step is to enhance the appearance for presentation and measurement (Fig. 14.3). Connectivity between voxels in, for example, a filament or a positively stained volume, may be selectively enhanced (the extracted structures may even be modeled as graphical tubes or solid objects; see SoftWorx from API and Imaris packages for examples). A threshold segmentation band can be interactively set to remove intensities outside the particular structure. 3D fill routines, 3D gradient, dilation, and other rank filters are the basis for structural object segmentation. Opacity (reciprocal to transparency) is possibly the most used visualization parameter to highlight structures segmented by intensity bands. This parameter controls the extent to which an object in the foreground obscures features situated behind it. Consequently, it artificially opposes the intrinsic transparency of biological specimens. Artificial lighting is applied during the final stage. Artificial material properties (such as opacity, reflectivity, shininess, absorption, color, and fluorescence emission) are all used to simulate real or macroscopic objects with shadows, surface shading, and hidden features.

Visualization for Multi-Dimensional Measurements

Often, the final requirement of objective visualization is the ability to extract quantitative measurements. These can be made on the original image, using the reconstructed views as aids, or made directly on the display views. The success of either of these methods depends on the choice of reconstruction algorithm and the objective control of the rendering parameters.

Table 14.2 gives an overview of visualization tools that might be useful for objectively exploring the image data (see also Chapter 15, *this volume*).

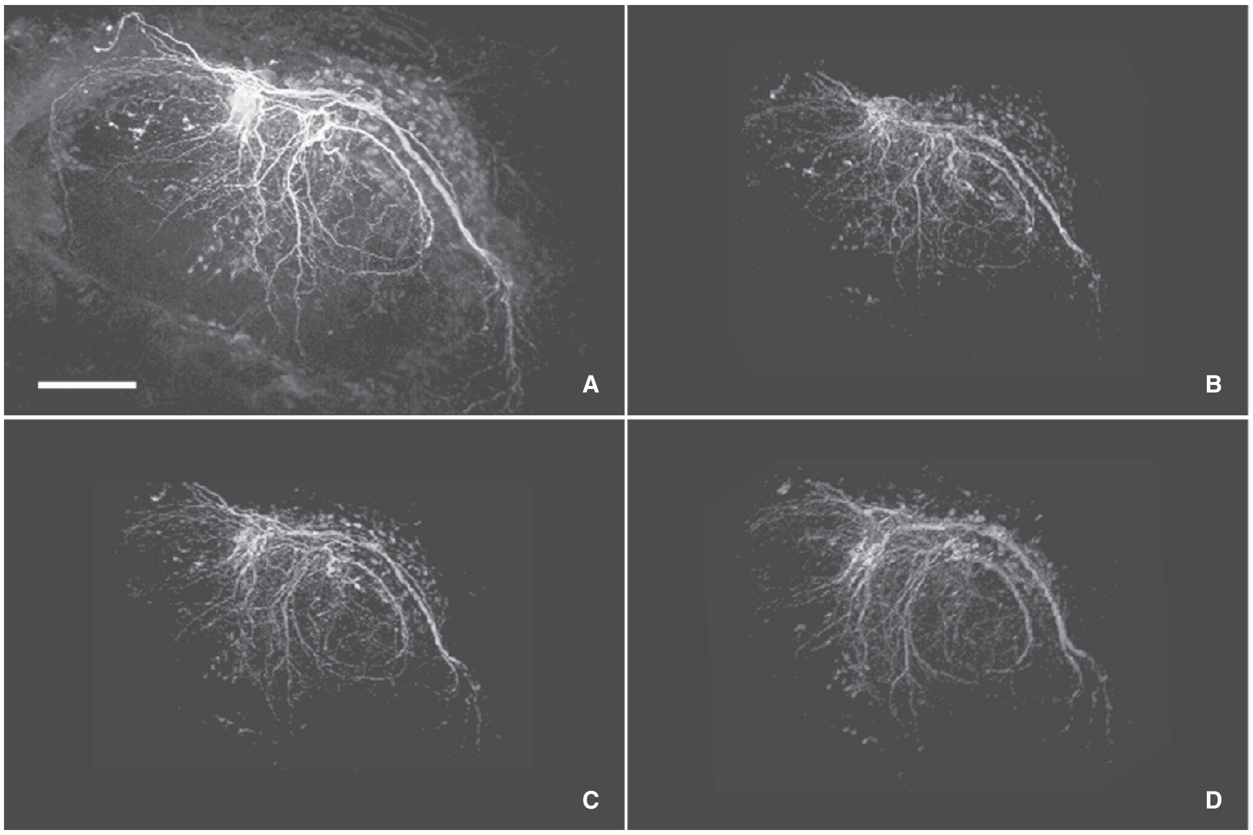

FIGURE 14.3. Enhancing and extracting objects. Having elucidated a particular structure within the volume, filtering and segmentation permit selective enhancement. (A) "Maximum intensity" view [as in Fig. 14.2(B)] after two cycles of alternate high-pass and noise-reduction filters on the original 2D *xy* sections (using 3×3 high-pass and low pass Gaussian filters). (B) More extreme threshold segmentation to extract the enhanced details during the projection. (C,D) two rotated and tilted views (Lasersharp software) using a "local average" (see text) to bring some "solidity" to the view. This example shows the principle danger of segmentation, that of losing fine details excluded from the intensity band.

TABLE 14.2. Overview of Visualization Parameters Desirable for Visualizing Multi-Dimensional Biological Microscopy Data

Processing step	Parameter	Minimum required	Desirable enhancements
[a]3D algorithms	General modes	*Xy*, *xz*, *yz* orthogonal slices *Z*-weighted "projections"	Arbitrary slices, Voxel α-blending Surface rendering
	Quick modes	Fast *xy*, *xz* slices Maximum projection	Hardware acceleration, Sub-sampling data
[b]Controlling the reconstruction process	Visualization parameters	Projection angles *z*-stretch Animation controls Sequence (movie) mode	Viewing angle, *z*-fill, Data threshold, Voxels/surfaces, Shading control, Lighting controls, Material properties, Opacity, SFP/"special" modes, Perspective, Batch processing, Post-lighting
	Pre-processing tools	2D & 3D image edit 2D image rank filter threshold/background contrast	n-D image edit, n-D filters, image restoration *z*-correction, morphological filters, math operations
[c]Interactive controls	Visualization parameters	Slice positions rotation angles data threshold animation controls	All render parameters, Data/view angles, View Zoom & pan, "Real time" control
	Measurements on image	2D measures on slices	3D measures on slices, n-D measurements
	Measurements on views		3D measures on views, n-D measurements
	Simultaneous measures on image & views	Multiple measurements on screen	Measures auto, Tracked in both displays

[a]The range of 3D algorithms indicates diversity of modes for tackling various kinds of image data, while the quick-look modes include general sectioning and the fastest voxel algorithms. Simple projections and section movies are always faster than more sophisticated reconstruction modes. [b]Control of the visualization process suggests the range of parameters that the user can modify directly to influence the resulting views. More controls give more flexibility but also more complexity in use.
[c]A very rough idea of the level of interactive control (i.e., rapid changes of the result in response to mouse clicks, etc.) for visualization and for measurements on source image data and/or reconstructed views. n-D = any number of multiple dimensions.

WHAT CONFOCAL LASER SCANNING MICROSCOPY IMAGES CAN THE VISUALIZATION SYSTEM HANDLE?

Image Data: How Are Image Values Represented in the Program?

Storing the Image Values

All digital microscopes produce image data values from analog-to-digital (A/D) converters. These will be packed into one or more 8-bit byte values, each of which may have an uncalibrated intensity range of 0 to 255. Greater collection precision is possible by integration, averaging, or other high-dynamic-range filtering operations. However, improvements in electronics and detectors now make possible the direct acquisition of 12-bit, 16-bit, or even higher precision digital data. Single-byte storage is more efficient, and is adequate, for the majority of purposes, particularly for results from low photon-flux imaging of living cells. It is supported by all packages. Some instruments allow 16-bit storage (a range of 0 to 65,535). Intensity data digitized by 12-bit A/D converters (standard in most current LSMs) is usually packed and unpacked into 16-bit words by the loss-less conversion:

$$I_{16} = I_{12} \times 16 + 15$$

This slightly cumbersome conversion is necessary to correctly rescale values in the range 0 to $(2^n - 1)$ without any rounding errors. The 16- to 12-bit operation is rapidly achieved by bit-shifting the binary 12-bit values towards the high byte and filling the additional 4 bits with 1 s. This operation can be precisely reversed for any integer value in the range. Sixteen-bit processing of original 8-bit or 12-bit data may also be desirable for derived images such as those from some fluorescence ratio experiments. However, this is excessive for the majority of confocal fluorescence images, which seldom record more than a few hundred photons/pixel and therefore have 10% to 20% shot noise (see Chapter 2, *this volume*). Microscopy image pixel values and views are economically represented by integer values. Permanent floating-point storage is rarely supported. Floating-point calibrations of integer data are discussed in the following section.

A distinction should be made between storage and display precision. Historically, some digital microscopy systems have used the display memory as both a recording and a view buffer with a built-in image or signal processor. Current approaches use a virtual display in main computer memory, which is copied to the display view, allowing decoupling of data and display view and greater storage precision than video memory if required. This is necessary, for example, for storing and displaying intermediate results in image restoration programs.

Image processing systems developed for cross-platform compatibility (see Amira, Image/volumeJ, and AVS examples of packages running over four platforms) have always used virtual displays allowing arbitrary precision images and views to be manipulated with as little as 5- or 6-bits of display depth per primary color. The price of this flexibility used to be a significant reduction in interactive visualization and display speed, caused by the loss of direct processor access to the video memory. One solution is to isolate platform-specific accelerations and link them to core routines when porting to high-performance workstations with non-standard hardware. Although this approach allows the rapid introduction of new proprietary hardware, it has now been almost universally superseded by the use of agreed platform-independent hardware standards with a defined software interface. Of the several contenders for a universal graphics standard the clearly adopted winner is the OpenGL scheme [see http://www.OpenGL.org and Woo (1999) for details of the OpenGL software programming interface]. This evolving scheme adds definitions for the handling of new technologies as they are introduced into each newly released OpenGL compatible display card or system.

Calibrating the Image Data Values

Multi-dimensional microscopy instruments provide the means for obtaining accurate and repeatable quantitative measurements. All parameters including calibration must be linked to the corresponding image for inclusion in subsequent processing stages. A discussion of file formats follows the section on image dimensions. Software packages normally use their own internal calibration structures because most of the general or so-called standard image formats do not support all the parameters necessary to fully describe multi-dimensional microscopy data.

It might be thought desirable to store directly calibrated real number data values. A fixed-precision mantissa and exponent would certainly provide consistent relative accuracy, regardless of the magnitude of the data values. Constant precision could, however, be maintained by using a logarithmic digitization (or detector) response. This is consistent with the fact that the presence of shot noise means that, if gray levels are separated by one standard deviation they must become wider as the signal level increases. More bits would then be assigned to low intensities and less to brighter values. A fixed precision (log) calibration could then be attached to the 8- or 16-bit integer data values. The minimum requirement is a floating-point offset (the real value of a 0 pixel), an increment (the real increment/pixel value), and at least a text label or key for the linear parameter represented [e.g., log (intensity), concentration, pH, etc.]. Nonlinear changes require a look-up table (LUT) for calibrations. Multiple-channel images require separate calibrations for each component. Ion imaging data need at least a fixed precision calibration and often a sigmoidal scale (defined by $R_{\min}$, $R_{\max}$, and K; e.g., Bolsover *et al.*, 1995). Table 14.3 summarizes data value calibration, arithmetic, and measurement requirements for a multi-dimensional visualization system.

What Dimensions Can the Images and Views Have?

Programmable scanning capabilities of all LSM instruments, motorized focus and/or *xy*-stage control of any microscope, and spectral or time-lapse capabilities yield images with a number of spatial, temporal, and other dimensions. Point-scanning LSM instruments normally acquire a temporal (sequential) and spatial (line) scan in the *x*-axis, repeated at further time points and optionally at progressive *y*- and/or *z*-axis positions. Hence, spatial and temporal sampling dimensions are simultaneously generated. In this way, *xy*, *xt*, *xz*, etc., 2D sections and *xyz*, *zyt*, *xzy*, *xzt*, etc., 3D volume images are collected. Time-lapsed volumetric (e.g., *xyzt*, etc.) or multi-channel spectral (e.g., *xyzc*, *xyct*, etc.) are examples of 4D images. Once considered no more than a curiosity by biologists, new dimensions of data are becoming routine. The possible five-dimensional (5D) (x, y, z, t, c) imaging space can now be augmented with *xy*- (stage) position (δx, δy, δz), spatial rotation (θ, ϕ, ν), lifetime (τ), polarization angle (P), polarization anisotropy (r). This makes 3D to 6D data (from 12 or more possible dimensions available on a given system) a routine target for data management.

Visualization systems need to support multi-channel images (Tables 14.3, 14.4, 14.6). Although ultimately, each channel is processed separately and the results merged together for display,

TABLE 14.3. Overview of Image Data Handling Features for Visualizing Multidimensional Biological Microscopy Data

Data handling feature	Parameter	Minimum required	Desirable additional enhancements
[a]Data storage	Types	byte	Integer, fp, real
	Bits	8, 24 (3 × 8)	12/16, 24 (3 × 8), 36/48 (3 × 12/16), n × 8
	Channels	R,G,B, included, Merge function	Arbitrary no. of channels n-channel merge
[b]Calibration of intensities		Linear, Offset, Range	Non-linear, Log, Sigmoidal, arbitrary
Intensity measures (distribution of pixel values)		2D Point, 2D Line	3D point, 3D line, trace,
		2D Arbitrary area	3D area (surface),
		Summed area volume	Arbitrary 3D volume,
		2D histogram	Results histograms,
		ASCII file output	DDE to Excel
Math operations		+,–,/,* logical, Contrast/gamma mapping,	Trig functions, Log
		Manual *z*-weighting	Auto *z*-weighting

[a] All systems support 8-bit (byte) data types. A few allow higher precision. This is useful for high dynamic range images. The use of 8-bit indexed or 16-bit "hi-color" modes for multi-channel data is now less common than 24-bit RGB support. Most scientific CCD cameras and LSMs now support 12-bit data (usually packed into 16-bit words) but few packages support these data types for visualization.
[b] It is important to clearly distinguish calibration of the intensity data values from the image dimensions (Table 14.4). Calibrated intensities also allow real values of pH, Ca^{2+}, etc. and other concentrations to be visualized.

visualization packages must now manage these parallel operations seamlessly in order to show multi-channel changes interactively. This is particularly important where interaction between the values across channels is required by the chosen algorithm (e.g., the Imaris SFP algorithm allows transparency in one channel to alter the simulated light emission from another fluorochrome channel).

Image editing is required to extract (1) subregions of a large data set or (2) a structure from the complexity of surrounding features. Sub-region editing should be available through each of the many possible dimensions of the data. All these dimensions must be appropriately treated, for example, correctly calibrated, if the results are to have quantitative validity.

Image Size

Maximum image dimensions should support the full resolution of the instrument (see Table 14.4). In extreme cases, several adjacent sections or even volumes may be co-aligned (by correlation and warping) and tiled together to form a single giant data set (e.g., Oldmixon and Carlsson, 1993). Generally, total image size should be limited only by the available memory. Virtual memory management provides transparent swapping of programs and data between RAM and disk. This increases run-time significantly but can enable very large data sets to be processed. Many software developers prefer to implement a proprietary mechanism of image caching or data swapping between RAM and disk, even with the built-in capabilities of the Windows family of operating systems. The best way to minimize these overheads is by careful crafting of the visualization algorithm. The plummeting price of RAM makes the use of ever more memory irresistible by the programmer, and thus inevitable by the end user.

Anisotropic Sampling

Most multi-dimensional microscopes are operated with different sampling steps in two or more axes. Visualization software must produce views with correctly proportioned dimensions and preferably have the ability to expand or contract each individually (Table 14.4), for example, artificially expanding the *z*-dimension of an image through a thin preparation (such as a biofilm or a stratified tissue) to highlight the morphology in each layer. The most concise way of specifying this aspect ratio information is to apply a correction factor to the appropriate axis calibration. This should be done interactively so that some imaging distortions can be corrected (e.g., for a specimen such as skin with layers of different refractive index). This does not change the data values in any way and is preferable to resampling the entire data volume, which would tend to use up precious memory. When the data is subsequently processed or displayed, a floating-point *z*-stretch parameter (and equivalents for *x*, *y*, etc.) would correctly specify the spacing of each plane. An integer *z*-fill parameter represents the number of equally spaced sections to optionally add between each of the repositioned planes. These extra data values are derived by interpolation, by pixel replication or linear, cubic, or higher polynomial spline. An obvious question arises here: How real are the extra data points? *A priori* knowledge of the specimen and imaging system is required for an informed choice. On-the-fly data expansion during processing will conserve storage space but requires more computations. Pre-expansion, for example, during the image loading cycle, will optimize processing speed at the expense of memory. A good compromise is rapid expansion during the computation using precalculated linear geometric LUTs.

Calibrating the Image Space

To make measurements, image and view dimensions must have the correct calibrations (Table 14.4). These must be updated during any resampling, zooming, and image editing. Minimum requirements for each dimension are again floating-point values for offset and increment, and an axis label. Warping conveniently handles nonlinear dimensions by resampling onto a rectilinear grid. Correction of acquisition errors should ideally be incorporated into a single intensity and sampling interpolation. These errors include:

- Spherical aberration caused by mismatch between the refractive index of the immersion medium, the imbibing medium and the design of the objective.
- Axial chromatic aberration (a focus shift seen with all objectives).
- Lateral effects, such as chromatic magnification error.
- Photometric signal attenuation and correction of geometric distortions from refraction within the sample (e.g., Carlsson, 1991; Visser *et al.*, 1991, 1992; Fricker and White, 1992; Hell *et al.*, 1993) are desirable preprocessing tools.

TABLE 14.4. Overview of Desirable Image and View Dimension Parameters for Visualizing Multi-Dimensional Biological Microscopy Data

Feature	Parameter	Minimum required	Desirable additional enhancements
[a]Image dimensions	Single plane	Full un-edited image (from camera, LSM etc), Held in RAM	Unlimited Display independent Multiple images in RAM
	Total image size	Fully sampled 3D image, 3D image in RAM	Unlimited, Display independent, Multiple 3D images in RAM, n-D images in RAM, efficient caching
	[b]Supported dimensions	2D, 3D *x,y,z* time	n-D, View angles, Rotation angles, Stage position, Polarization/anisotropy, Lifetime
Editing the dimensions (geometric operations)	Sub regions (ROI)	2D sub-area, 3D sub-volume, edit on slices	3D arbitrary sub volume, Edit in view, 3D cut-away, n-D ROI
	[c]Data corrections	Background normalization *z*-atttenuation	Non-linear corrections, Photobleaching, Flat field, n-D corrections, Optical corrections, Image restoration
Z-geometry	*z*-stretch	Integer value linear	Real value Non-linear (e.g., cubic, etc.)
	z-fill	Integer for large angles	Adaptive for chosen angles
View dimensions	Single view	3D diagonal of image View movie in RAM JPEG compression	Unlimited, Display independent Multiple views in RAM Efficient caching, Efficient compression
	Number of views	120 views (360 × 3 degs)	Unlimited, Display independent Multiple movies in RAM
	Channels in view	R.G.B	Arbitrary no. of channels
[d]Calibration of dimensions	Image	*X,y,z,t*	All dimensions
	View	*X,y,z,t*,angle	All dimensions
Dimension measures	On image	2D Point, 2D Line, 2D histogram, 2D Arbitrary area, ASCII file output, Summed area volume,	3D point, 3D line, trace, 3D area (surface), Arbitrary 3D volume, Results histograms, DDE to Excel
	On view		3D point, 3D line, Trace, 3D area (surface), Arbitrary 3D volume, Results histograms DDE to Excel

[a]In most cases the image data space is limited only by the amount of disk and/or memory available. The operating system and/or the application program may provide virtual memory management and disk caching.
[b]Most packages can handle time, spectral, etc., data as for a "*z*-stack" but few can directly interpret time or wavelength calibrations with any meaning.
[c]Complex corrections usually involve sample-specific data and some pre-processing.
[d]Calibration of dimensions should be clearly distinguished from those of the data intensity values (Table 14.3).
n-D = any number of multiple dimensions.

Standard File Formats for Calibration and Interpretation

While there are many standard formats, there is no universal standard currently adopted for microscope images. However, there are established imaging formats (e.g., DICOM, see http://medical.nema.org/) that are routinely used by visualization packages such as the Cedara, Vital Images, and Analyze software that fully describe multi-dimensional volume data from medical scanners. As LSM and other research microscopes become more routinely used as screening instruments and for clinical applications, it is hoped that such standards will become routine from these suppliers as well. A catch-all image input facility such as the RAW options offered by many programs allows any packed binary file with a fixed-size header to be read in. Microscope instrument manufacturers have taken one of two options: (1) developed a completely proprietary structure and made this available to other developers and users, or (2) taken an existing extendable format (such as the Tagged Image File Format [or TIFF]) and added system-specific components (e.g., for TIFF, licensed specific tags) to store the extra acquisition parameters. A problem with this second approach is the necessary proliferation of a number of variants or compliance classes of such formats. Any third-party reader program must recognize (and provide updates for) several different versions. A widely adopted alternative is to use a proprietary structure and to provide conversion tools to import/export data via standard formats. Unsupported parameters are transferred into the program by an *ad hoc* semi-manual process.

A flexible, industry-standard approach to image-related details is to use a conventional database to store preprogrammed fields of information (sometimes a third-party software product is used with the visualization tool — such as the ImageAccess database used by Imaris — which can manage all image and image-related files). Two types of information must be stored and linked with each image: (1) instrument-specific details describing the instrument settings used for the collection and (2) image-specific information describing the dimensions, calibration, and experimental details. The database can hold both sets of details, together with a pointer to the image data (or even the image data itself for small images). Alternatively, the database may hold just the system configurations used as stored settings or methods (e.g., the Bio-Rad Lasersharp program stores all the instrument and user settings in a Microsoft Access database). This latter approach requires a pointer to the relevant settings to be saved with the image data, separately from the database. Table 14.5 summarizes some important image and view data parameters.

Processing Image Data

Less obvious than the storage representation are the data type and precision used during computations. Floating-point representations

TABLE 14.5. Overview of Desirable File Format and Image Information Features for Visualizing Multi-Dimensional Biological Microscopy Data

Feature	Parameter	Minimum required	Desirable additional enhancements
[a]Image file format	Proprietary standard	Fully defined open source Multi-file TIFF, AVI (for series)	Fully defined open source, Full range of conversions, A Universal standard!
View file format	Proprietary standard	Fully defined open source Multi-file TIFF/BMP, JPEG, AVI	Fully defined open source, Full range of conversions, Efficient compression, A Universal standard!
[b]General params. stored	Size	All dimensions	All dimensions
	Calibration	*X,y,z,t* dimensions	All dimensions
	Annotation	ROIs	ROIs, Text, pointers
	Microscope	Data specific parameters Stored in image format, or ASCII file	All instrument parameters, Experimental parameters, Stored in image format and/or database
	Notes		User/exp notes, Informatics
Special view parameters stored	Source image		Image filename, Links in database etc., Visualization history/log
	Orientation etc.		Rotation angles, etc.
	Visualization parameters		Algorithm name, Algorithm parameters, Display options

[a] Proprietory file formats are used by most systems. "Standard formats" such as TIFF may also cause confusion as there are many different compliance classes of TIFF, so only a sub-set of the TIFF tags in a particular file may be recognized by a given reader.
[b] Some parameters may be stored with the image data in the same file, in a separate (e.g., ASCII) file or in a database. It is important to know the whereabouts of this information if the image is to be taken to another program with the associated data intact. ROI = region of interest.

reduce rounding errors during geometric transformation interpolations. Even this requirement for floating-point representation can be partly avoided by either (1) combining several interpolation steps into a single, composite geometric and photometric transformation, or (2) increasing the sampling by a factor of at least 2 for each subsequent interpolation. This second approach is somewhat extravagant in terms of storage and will not help if the sampling is already at the Nyquist limit. The processor architecture is an important factor in determining the processing speed. Fast multi-word and floating point arithmetic is now standard in microprocessors. Despite this, some instruments, notably the Zeiss range of LSMs, use specialized, programmable digital signal processors.

Processor Performance: How Fast Will My Computer Process Images?

Personal computer (PC) performance for image manipulation is constantly improving, making the specification of system performance in a text such as this somewhat pointless. However, the principal components of the computer system required can be described in terms of their relative importance to performance.

At the time of writing, the Pentium PC processors are the norm, running at around 4 GHz with bus speeds around 1 GHz. These are very approximately 30 times faster than 10 years ago, representing a doubling of speed every 2 years. Non-Intel processors with alternative combinations of price/performance through low power consumption, higher capacity of on-chip memory for data caching, and other enhancements appear from time to time with advantages in different applications. Alternative Intel processors, such as the Xeon, also compete in these areas and offer improved workstation and multi-processor performance. Provided the software is correctly designed, transfer bottlenecks can be reduced with a processor having at least 512 kB of level 2 memory cache. Apple Macintosh machines have undergone something of a renaissance in recent years; the current G5 is broadly equivalent to the latest Pentium devices, and still have competitive and equivalent components for efficient numerical performance and a highly optimized bus for image transfers. The current Macintosh OS X operating systems have been significantly updated and based on Unix technology in order to take advantage of the large software developer base. Unix workstations are still a costly alternative to ever-improving PC platforms. Improving processor performance alone is still reflected in the voxel rendering performance (in voxels/second or vps) for visualization of multi-dimensional microscopy data.

Improvements in other areas of the PC have been either necessary to keep pace with the processor speeds or provided enhanced capabilities directly. Hard disk drive data transfer speed can limit the speed of animations (movies) and 3D visualization when applied to large data sets. At the time of writing, so-called ultra-fast, ultra-wide SCSI interfaced devices, with capacities up to 250 Gb per disk still have higher performance than IDE devices and tend to be more robust and easier to upgrade, although plug-and-play technology makes this last issue less important in the latest PCs. The latest PCs and Macintosh computers can access 4 to 8 Gb of RAM. This is adequate for most multi-dimensional data sets but will inevitably still limit performance if many large data sets are opened simultaneously, especially if the software is designed to read in the entire data set and/or the system caching or swap file is inefficiently configured for the ratio of disk to RAM.

Computer video display subsystems have, over the last 10 years or so, taken on more and more graphics processing operations, allowing greater optimization and relinquishing the general purpose CPU for other tasks. The display system has become a dedicated graphics processing unit (GPU) and up to 256 Mb of dedicated display memory. Some entry-level PCs may still use portions of main memory, set aside for access by the display, but these are not recommended for multi-dimensional visualization. Many functions are carried out by dedicated hardware and/or firmware running on the GPU and associated devices. Depending on the sophistication of the chosen graphics system, supported operations may include:

- Rapid display of 2D views for animations, etc.
- Rendering of surfaces composed of triangle or other polygon primitives.

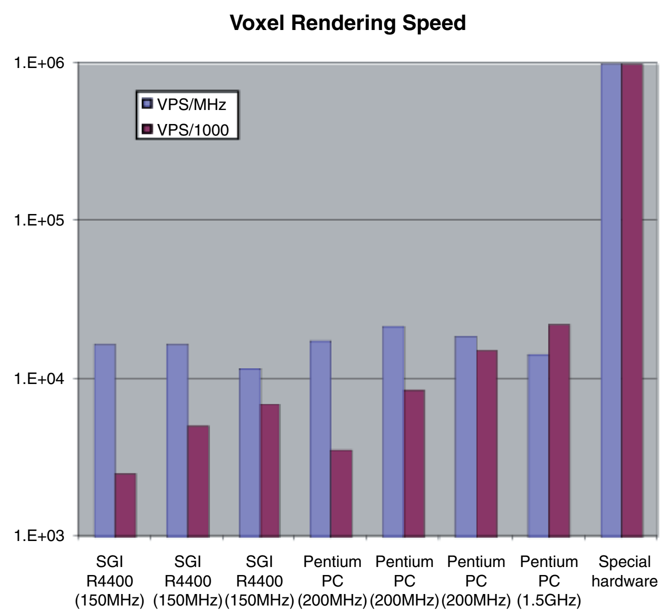

FIGURE 14.4. Voxel rendering speed: dependence on hardware performance. When assessing a visualization system, many factors need to be taken into account (see text). Parameters for individual performance figures should be assessed with care. On standard platforms, processor speed is still an important factor. From a simple ratio of voxels processed per second per MHz processor speed (with a basic algorithm) a figure of merit can be obtained. Running the same α-blended. voxel-rendering software (Voxblast) on multiple Pentium processors gives broadly the same figure of merit as single processors when normalized for the total processor speed. The same is found for multiprocessor graphics workstations. Running on special hardware (this example is the VolumePro board) sacrifices portability across platforms but (as has historically always been the case) gives vastly improved performance.

- Geometric manipulations (e.g., warping of data vectors).
- Rendering of voxel objects.
- Transparency/opacity of graphics and voxel objects.
- Artificial lighting and shading.
- Rapid manipulation of color or grayscale.
- Panning and zooming of the display.
- Texture mapping (used to rapidly render image layers onto a growing display view).

Figure 14.4 shows some approximate voxel rendering speeds that might be expected over a range of processing platforms (data corresponds to rendering speeds of Voxblast from Vaytek Inc.). Optimization of the GPU functions is controlled largely by the supplied driver software and contributes to the major differences between various hardware configurations. CPU operations are coded by the application programmer and this is also reflected in the performance of the software. The relative efficiency of these two aspects can have an important influence on the effectiveness of the package as a whole. An effective visualization algorithm for multi-dimensional data must include optimized numerical loops (particularly nested sequences) and use fast indexing into preprocessed parameter LUTs for frequently used values. The following section describes some of the optimizations that are responsible for the performance range seen between different programs.

HOW WILL THE SYSTEM GENERATE THE RECONSTRUCTED VIEWS?

Assessing the Four Basic Steps in the Generation of Reconstructed Views

(1) The image (or a subregion) is loaded into the data space (an area of computer memory). Preliminary image editing, preprocessing, and/or analysis is used to define calibrated image values with known dimensions. This constitutes the input to the visualization process. Packages such as Analyze have some useful preprocessing capabilities (Robb, 1990). Alternatively, a more general program such as Metamorph, ImageJ, and Image Pro, etc., can be run alongside the visualization package for image preprocessing (or the visualization component can be added to the 2D package).

(2) A view must be chosen (subject to the available reconstruction algorithms) that will produce the most flexible and appropriate representation of the image data. An intelligent choice of view can minimize the number of reprocessing cycles (see also He *et al.*, 1996; Marks, 1997; Kindlmann and Durkin, 1998, for attempts at computer-assisted choice of visualization algorithm). The visualization step consists of two transformations: First, a geometric orientational mapping of the image space into the reduced dimensions of the view, and, second, a photometric mapping (sometimes called a transfer function) whereby the image intensities are processed to determine the brightness of a pixel at each position within that view.

(3) The display step consists of a second geometric and photometric mapping that together constitute output or matching of the multi-dimensional view into the available physical display. In practice this may consist of scaling and copying or a more complex operation (e.g., animation or stereoscopic presentation). These presentation or output options, dictated by the display space capabilities, will determine the most efficient use of screen resolution, color, animation, etc. In turn, these will influence the choice of appropriate reconstruction algorithm.

(4) Dimensional loss during the visualization processing is partly restored by the display step and partly by *a priori* knowledge used to interpret the 2D display view (e.g., depth cues, animation, stereo, etc.). Inspection and analysis of the display view is the last step of the visualization process.

The next sections describe more details of these processes that are important for microscopy images using techniques found in the systems listed in Table 14.1.

Loading the Image Subregion

Any image processing program must first open the image file, read and interpret the file format information, and then load some or all of the data values. Interpretation of the file format largely determines the flexibility of subsequent manipulations. An on-screen view of (1) image sizes (in pixels and calibrated units), (2) intensity data calibrations, (3) associated notes and (4) a quick-look reconstruction will aid selecting the required image or subregion (Analyze and Imaris, e.g., show image volumes as thumbnail pictures with a grid showing the image dimensions, etc.). The file format information will determine whether the data needs resampling to produce correct image proportions, and interactive adjustment is essential for *z*-stretch/fill (see above). Interactive photometric rescaling or segmentation (in combination with a simple volume representation) are essential to remove (e.g., set to zero or ignore) background values that would unnecessarily slow down computations. Multiple passes through the data will be time consuming for large images. A single composite geometric and photometric resampling (using fast LUTs) should be combined with loading the data from disk. Data expansion options (e.g., *z*-fill) may be temporarily restricted to speed up computations during the exploratory stages. Flexibility and control at this stage must be balanced against the efficiency of a single processing stage. Some image preparation options are detailed in Table 14.2.

Choosing a View: The 5D Image Display Space

As introduced above, the efficient use of all the available display space greatly increases the flexibility of visualization algorithms.

The 2D Pixel Display Space

Pixel resolution must accommodate a reconstructed view at least as big as the longest diagonal through the 3D volume. This means that, for example, to reconstruct a 768 × 512 × 16 frame 3D image with *z*-stretch of 4 and arbitrary rotation, the display view that will be generated in memory could be up to 950 pixels square. For the same computation and display of 1024 × 1024 pixel frames, 1450 pixels square are required to avoid clipping. As it is advisable to display the views without resampling, these values represent the minimum display window in pixels. Processing time may dictate that only a subregion can be processed but, in general, display of a single full resolution frame should be considered a minimum. Although the display pixel range may be only 8 bits/channel, the ability to generate projected views with a higher intensity range (perhaps 16 bits) means that, for example, average projections of images with dimensions greater that 256 pixels can be made with no loss of detail. It is now standard practice to produce an output view that is independently rescaled according to the size of the display window as defined by the user. This is transparently handled by the software and display driver. However, rescaling can always give rise to unwanted aliasing effects so it is wise to restrict the display zoom to integral multiples of whole pixels. The application program, perhaps using features of the display driver, may allow an image of greater size than the physical display to be rapidly panned, giving access to display views of almost unlimited size. High-resolution non-interlaced displays are now standard for all computers. Although a single display may deliver resolutions up to 2650 pixels, it is now standard practice to provide multiple screen outputs from the best display systems. In this way, desktops of perhaps 2560 × 1024, 3200 × 1200 or more can be spread seamlessly across a pair of similar monitors placed together. The display drivers will automatically handle traversing of the mouse and program windows between the physical screens or even allow large images to straddle the entire display space. (A commonly recommended supplier of multi-view compatible OpenGL graphics cards for PCs is nVidia, http://www.nvia.com, while on Macintosh's they are built in.)

The Color Display Space

Color is a valuable resource for coding multi-dimensional information on a 2D device. It is important to ascertain the number of different colors that can be simultaneously displayed, as distinct from the number of possible colors present in the data or display view. The author prefers the generic term **palette** to represent the subset of simultaneously displayable colors and **color resolution** to indicate the full set of possible colors present in the data. Although many different graphics display resolutions have been used by imaging systems in the past, the plummeting cost of hardware have made the use of all 8-bit displays redundant. Useful display systems will be encountered that have either 16, 24, or 32 bits per pixel of display depth. It should be carefully noted that a display system may have additional memory associated with each pixel for storing other values important for controlling the display process, but here we are concerned only with the color and intensity information. A standard 24-bit display has 8 bits of memory storing 1 of 256 possible values each of red, green, and blue intensity. Additional display panes are available in 32 bit modes. With 2^{24} possible display colors (over 16 million), a 4000 × 4000 pixel image could display each pixel with a different and unique color. There is, therefore, significantly more contrast available in a color image than in a monochrome (e.g., grayscale) representation. However, it must always be remembered that the actual red, green, and blue colors corresponding to each component are fixed by the spectral characteristics of the physical screen material. These will, in general, never coincide with filter spectra of the microscope, or even with the nominal red, green, and blue characteristics of a color camera.

When more than 24 bits of data are stored for each pixel of the display view, such as for a 3-channel 16-bit color image (a 48-bit data set), the visualization software must resample this down to the available color space of the display system. An extreme example is the option in the Imaris program of having color-space computations carried out with 96-bit precision as opposed to 24-bit precision, improving accuracy at a 4-fold cost in extra memory. However, at present cathode-ray tube (CRT) and liquid-crystal displays (LCD) are capable of displaying little more than 8 or 9 bits of data in each color channel.

Pseudo Color

Pseudo or indexed color was used by older 8-bit displays. It is now only really important when a display system of very high resolution is implemented, for cost purposes, with 16 bits of high color pixel depth. Each of 65,536 entries (for a 16-bit mode) or 256 entries (for 8-bit modes) in a color look-up table (CO-LUT) is assigned a unique composite RGB value. This CO-LUT is an indexed palette and can be rapidly updated or modified to change the displayed colors without altering the view data values. It is the CO-LUT value pointed to by each data value that determines what RGB intensities appear on the monitor. Visual perception of color is far more acute than for intensity in bright VDU displays because cone density in the eye is highest in the fovea (Perry and Cowey, 1985). Pseudo color is, therefore, useful for presentation of calibrated 16-bit maps of image intensities, for example, from ion indicators. In general, it adds contrast to subtle changes in (1) brightness, (2) temporal, or (3) coordinate (typically *z*-relief) views.

True Color

True color means any display element can have independent values for each of its red, green, and blue components. The simplest way of representing these in a byte-structured format is a 24-bit (3 × 8 bit) RGB voxel. Other color-coding schemes are possible. Hue, saturation, and brightness (HSB) are useful for intensity-independent color transformations. Process color space (using cyan, magenta, yellow and black — CMYK) is the form used for hard copy and publication. RGB values map directly into a 24-bit display with no intermediate processing. Color manipulations can be carried out by modifying the component color data directly. Alternatively, each 8-bit channel may be driven by a monochrome (R, G, or B) 8-bit indexed CO-LUT (palette).

Multiple-Channel Color Display

Either color or brightness resolution (or both) can be traded for extra channels. A hue (preferably non-primary, i.e., magenta, cyan, yellow, orange, etc.) is defined by a unique RGB ratio for each channel. An intensity (brightness) scale in each hue then represents the indexed data values of that channel. All channels are combined into one true-color RGB view, adjusted to fit the display resolution, that is, each channel using a segment of the available palette. Figure 14.5 includes examples of the use of color for 3D multi-channel and stereo display.

Animations

As with pixels and color, the temporal display space can also be effectively used for visualization. The simplest temporal mapping is the sequential display of view sequences. Temporal range is determined by the number of frames that can be stored for rapid animation. Time resolution has two components: the frame rate (the time between successive views) and the refresh rate (how fast a single view is updated) (Table 14.6). The refresh rate contributes significantly to the perception of smooth animation. Retinal persistence results in a screen refresh rate of ≤1/18th of a second being perceived as virtually instantaneous. For through-focus sequences, fading between frames is advantageous. A long-persistence display phosphor (such as on older video-rate monitors) assists this fading process for low framing rates ≤4 Hz but contributes degrading blur at higher speeds. Perception of smooth motion requires high lateral resolution and visual acuity. Therefore, smooth rotation animations require (1) fine rotation steps, (2) a short persistence/high refresh rate display, and (3) an animation frame rate of above 10 Hz (with ≤0.05 s data refresh). Hardware and software compression/expansion (see Chapter 48, *this volume*) are built into some display systems, allowing suitable data to be animated at up to video rate with reduced storage requirements. Both RAM-based and hard-disk–based systems can now easily provide full-color video-rate animation. Screen update is improved by a double-buffered display comprised of both a visible and a

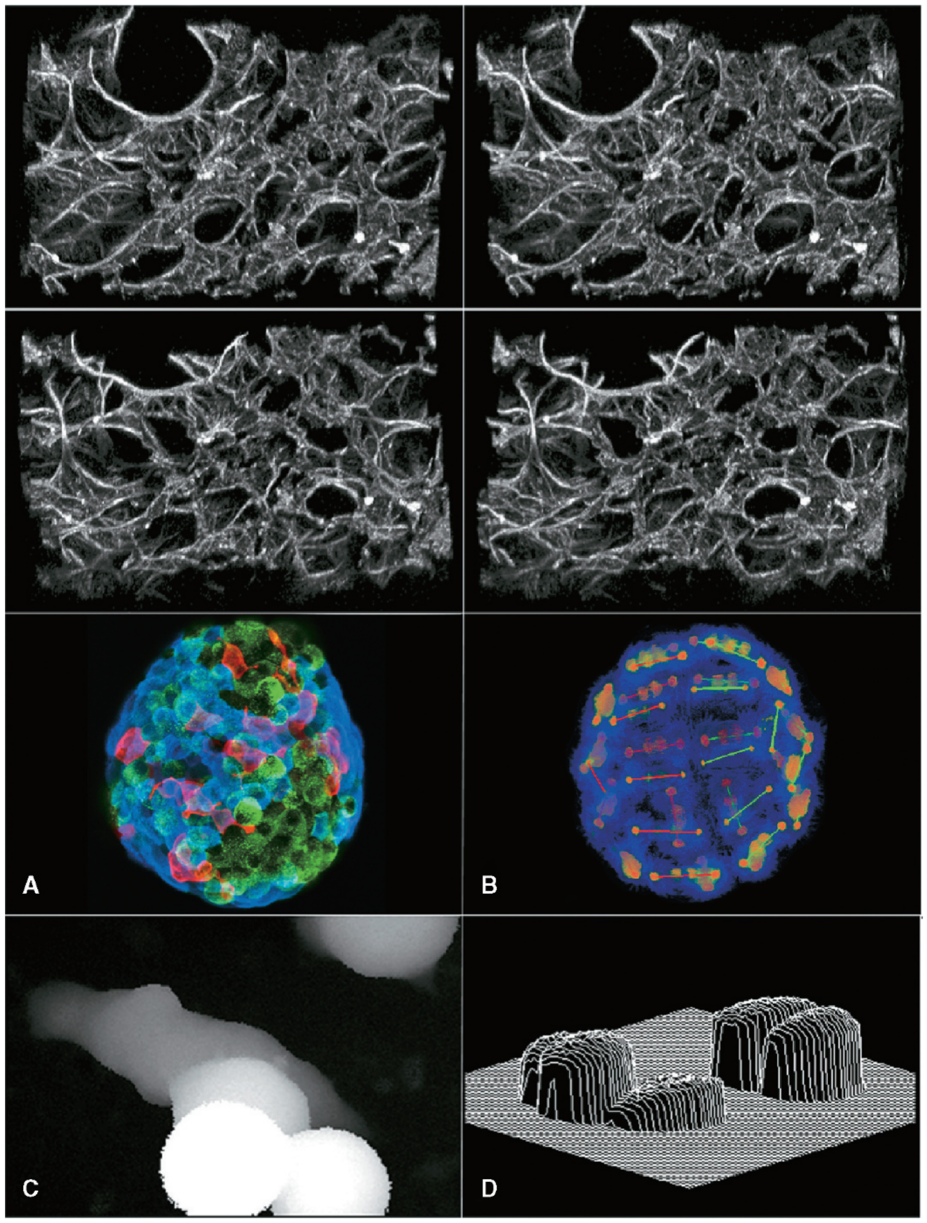

FIGURE 14.5. Efficient use of the 5D display space. The upper four images are two "maximum intensity" stereo-pairs (Lasersharp software). They were generated with ~8 deg of "rotation" around the *y* (vertical axis) giving binocular stereoscopy through the *x* display dimension and similar "tilts" around *x* to give motion parallax and temporal interpolation depth cues using the *y* display axis. In these static views, the top pair tilt forwards and the lower pair tilt backwards. With few exceptions, the most efficient use of the color space is for the display of multi-channel views. Data (courtesy of Bio-Rad Microscience) is from a large confocal series from lung tissue. (A) shows a triple-stained fluorescently labelled pancreatic islet, with each channel "maximum projected" and combined into a 24-bit Windows bit-map view (data collected by T.J. Brelje, University of Minnesota, Minneapolis, MN). (B) shows a dividing shrimp embryo stained with rhodamine-conjugated beta-tubulin antibody (27 five-micron optical sections) rendered using VoxelView/Ultra. Cell bodies and membranes (blue) are assigned low opacity so that microtubule structures (orange-red) can be viewed distinctly in their cellular context. Analytical geometric data (lines and surfaces) can also be inserted, not overlaid, using the VoxelView/Ultra Embedded Geometry tool. Embedded lines highlight the axes of division and centers of polarity of the dividing cells and help indicate directions of movement during mitosis. (Data courtesy of Dr. W. Clark, Jr., University of California, Bodega Marine Laboratory, CA). Intensity gray levels can also code for *z*-depth (see text). (C) shows a Lasersharp "height" view of a living fibroblast imaged by fluorescence optical sectioning of an excluded FITC-dextran-containing medium (see Shotton and White, 1989). (D) Binary (single-bit) line graphics make inefficient use of display space. However, this "YMOD" or height profile of BCECF-stained living chondrocytes from pig articular cartilage (data by R.J. Errington, Physiology Dept., Oxford University) does show relief more clearly than would an intensity view alone.

TABLE 14.6. Overview of Image and View Display Options Desirable Visualizing Multi-Dimensional Biological Microscopy Data

Feature	Parameter	Minimum Required	Desirable additional enhancements
[a]Display 2D pixel size		To show full image 1 : 1 without clipping (typically needs 1280 × 1024 or more)	As large as possible, Multiple-screens, Seamless desktop
Color	Display mode	24-bit RGB	24-bit of higher + overlays
	[b]Multiple-channels	Standard RGB	Arbitrary number of channels
Screen	Display refresh (Hz)	70 Hz	~100 Hz
	[c]Size (diagonal inches)	CRT: 19 Flat: 17	CRT: multi 21, Flat: multi 19, Wide-aspect & Specialist Mega-pixel screens
Movie	[d]FPS (Hz)	~10 at full image resolution Variable fps	Up to about 30 fps, Motion compression, Variable fps
	Recording	Store movies as digital file	Digital video store, Digital Compression, DVD recorder, DVD RAM
	Hardware assisted		z-buffer video system, Compression AV quality disk system
Stereoscopic	Modes	Manual stereo pairs Movie pairs Anaglyph display	Side-by-side, LCD viewers, Shuttered screen, Projection, Non-viewers (e.g., lenticular) Standard hardware (e.g., OpenGL)
	Animation	2 color anaglyph	Full color Auto stereo from 6 deg sequence

[a] Most operating systems and application programs decouple the image size from the display size. If the image must be sub-sampled by the system to display in the chosen window, aliasing may occur (some graphics systems have anti-aliasing devices built in). Usually, not all of the screen area is available for the image, so the screen needs to be bigger than the largest image. Some graphics systems allow an image larger than the screen to be "displayed" and the visible part is panned around with the mouse.
[b] With color-space mixing, it is possible to "merge" an arbitrary number of channels into a standard 3-color, RGB display.
[c] CRT sizes are usually given as the tube diagonal, not the visible screen size, flat panel displays indicate the actual viewing area.
[d] The animation software must be highly optimized to deliver the fastest, smoothest framing rates. This can be achieved in software at the expense of standardization and so the fastest systems may only work with a limited range of display hardware.
FPS = frames per second. LCD = liquid crystal display.

second (non-displayed) buffer. The second buffer is updated while the first is read out to the monitor and pointers to the two buffers are switched between successive frames. New graphics standards, especially OpenGL, now fully support double buffering on standard displays. Double buffering obviously needs twice the memory on the display card.

Stereoscopic Display

Depth perception by stereo parallax provides a third spatial display dimension. Some of the geometric *z*-information can be mapped into this stereo space. Like the color/intensity range compromise, the stereoscopic depth requires some reduction in bandwidth of another component. The two halves of a stereo-pair can be displayed using screen space components normally reserved for (1) 2D pixel area, (2) color, or (3) sequences (temporal space). Each of these methods requires an appropriate viewing aid to ensure that each view is presented only to the appropriate eye. The detailed implementation of stereo presentations are described in a later section. Table 14.6 shows some image and view display options for visualization systems.

Optimal Use of the 5D Display Space

Several conflicting factors must be balanced: (1) visual acuity in a particular display dimension, (2) efficient use of display resources, and (3) minimizing processing time. Because intensity variations are difficult to interpret in a low-contrast image, it is sometimes tempting to use *y*-mod geometric plots and other display tricks to represent, for example, a fluorescence ion concentration. Using the geometric space rather inefficiently in this way for a simple intensity display may allow us to view inherently planar information with greater accuracy. A contrasting example might be when a depth profile surface can be defined from a 3D object: (1) the geometric space in *x*, *y*, and *z* (e.g., stereo) could be used to show the object's surface relief, (2) color used for material properties (fluorescence, reflectivity, etc.), and (3) intensity (grayscale) employed to reinforce *z*-cues by depth weighting. Automontage is an interesting application (from Syncroscopy, Ltd.) where surfaces are extracted by ray-casting projections of widefield *z*-focus series. The resultant 3D data is then visualized using *z*-profile plots or stereoscopic views.

The best display space for a particular component will depend on the available resolution and the range of the data. In general, multi-channel images are best shown as different colors, in which case depth information must be coded using stereo or motion parallax or some lighting/shading mechanism. Binocular stereoscopy works for views rotated around the *y*-(vertical) axis when looking at the screen, that is, with parallax shifts in the horizontal *x*-direction (Frisby and Pollard, 1991; Poggio and Poggio, 1984) (for an upright observer!), while motion parallax is perceivable around any axis within the *xy*-plane. The perception of depth by so-called motion parallax is actually a subconscious interpolation of the images between each view to fill in the path of features presented at discrete loci along a simple trajectory (Nakayama, 1985; Fahle and de Luca, 1994). Therefore, a sequence of side-by-side stereo-pairs at increasing tilt angles only will give stereo depth in *x* and animation depth in *y* with minimum processing. Rotations are interpreted more readily by most observers than other temporal sequences, such as through focus *z*-series, largely because of our acute perception of parallax. Detailed assessment of particular presentation modes requires an in-depth knowledge of the physics and physiology of visual perception (e.g., Braddick and Sleigh, 1983; Murch, 1984; Landy and Movshom, 1991). Alternative temporal coding strategies, such as color-coded tixels (Kriete and Pepping, 1992) thus aid the presentation of non-rotated time series, particularly if interactive measurements are to be made. Figure 14.5 shows examples of the efficient use of display space for multi-dimensional display.

Mapping the Image Space into the Display Space

Having chosen both the image dimensions and display space, a suitable mapping of image space to the output view dimensions must be found. Choices for this geometry processing are intimately linked to the implementation of the transfer algorithm for combining the data intensities, however, it is more useful to consider these components separately in order to make the most of available resources; geometry and intensity processing software and hardware may reside in different subsystems of the visualization workstation.

For a general multi-dimensional image $I(x_i, y_i, z_i, t_i, c_i, \ldots)$ and view $V(x_v, y_v, z_v, t_v, c_v, \ldots)$ we can define an overall reconstruction function (R) such that

$$V(x_v, y_v, z_v, t_v, c_v \ldots) = R\,[I(x_i, y_i, z_i, t_i, c_i, \ldots)] \qquad \textbf{(1)}$$

where x, y, z are the spatial coordinates, t is time, c is color channels, etc.

R has two components: a geometric transform (G) converting image to view dimensions and a compositing (sometimes called transfer function) or projection operation (P) performed on intensities through the view space (Fig. 14.6). These components of R are thus related by

$$V = P(x_v, y_v, z_v, t_v, c_v, \ldots)$$
$$\text{where } x_v = G_x(x_i, y_i, z_i, t_i, c_i, \ldots),\ y_v = G_y(x_i, \ldots) \text{ etc.} \qquad \textbf{(2)}$$

The following sections describe various G functions used in visualization systems (listed in Table 14.7). Projections are described later (and listed in Table 14.8).

Simple Visualization: Reducing the Geometric Dimensions

This involves discarding all but two of the voxel coordinates and mapping the remaining dimensions to screen xy-positions. A non-rotated **orthoscopic** (non-perspective) view of a 3D (x_i, y_i, z_i) volume (viewed along the z_v-axis) is a simple geometric mapping of serial sections that can be projected (e.g., by summing, maximum intensity, etc.) onto a 2D orthogonal $(xy)_v$ display (Fig. 14.6). The G function is defined by

$$x_v = x_i,\ y_v = y_i,\ z_v = z_i, \text{ i.e., } V(x_v, y_v) = P(x_i, y_i, z_i) \qquad \textbf{(3)}$$

For a 3D time series (x_i, y_i, t_i) to be viewed edge-on, (x_i, t_i), the transformation is equally simple:

$$x_v = x_i,\ y_v = t_i,\ z_v = y_{i\text{i.e.}} \quad V(x_v, y_v) = P(x_i, t_i, y_i) \qquad \textbf{(4)}$$

These are the basis of the familiar three-pane orthogonal section views found in many visualization programs.

Rotations

A single, orthoscopic, x-axis rotation (θ) requires a geometric mapping given by

$$x_v = x_i, \quad y_v = y_i\cos\theta + z_i\sin\theta, \quad z_v = -y_i\sin\theta + z_i\cos\theta \qquad \textbf{(5)}$$

then $$V(x_v, y_v) = P(x_v, y_v, z_v)$$

The projection is then performed in the (re-oriented) view coordinates. Offset coordinates (i.e., $x_i - x_o$, etc.) are used for rotations around a point (x_o, y_o, z_o) other than the image center. Rotations are non-commutative, that is, the order of x-, y-, and z-axes matters. The observer's coordinate system (x_v, y_v, z_v) is static, and all orientations are given in this frame of reference. To generate a view of the image rotated simultaneously about the three image axes (i.e., a tumbling algorithm), three consecutive transformations are required. The first [e.g., a tilt around x_i, Eq. (5)] is obviously

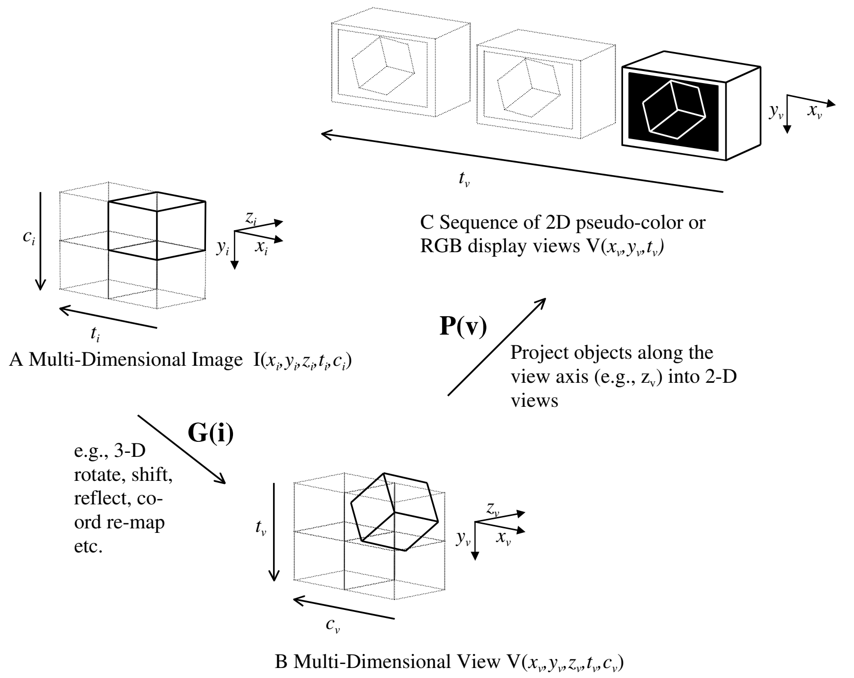
t_v
y_v
x_v
C Sequence of 2D pseudo-color or RGB display views $V(x_v,y_v,t_v)$
c_i
z_i
y_i
x_i
t_i
A Multi-Dimensional Image $I(x_i,y_i,z_i,t_i,c_i)$
P(v)
Project objects along the view axis (e.g., z_v) into 2-D views
G(i)
e.g., 3-D rotate, shift, reflect, co-ord re-map etc.
t_v
z_v
y_v
x_v
c_v
B Multi-Dimensional View $V(x_v,y_v,z_v,t_v,c_v)$

FIGURE 14.6. The visualization process. Voxel and object visualization algorithms proceed in three clear steps: (1) Multi-dimensional image space (A) is transformed by a geometric function (G) to the (re-orientated) view space (B). (2) Selected objects in the view space are combined using a projection operation (P) to produce a sequence of 2D views. (3) The 2D views are presented on the display device (C).

TABLE 14.7. Overview of Image-to-View Space (Geometric) Transformations for Visualizing Multi-Dimensional Biological Microscopy Data

Feature	Parameter	Minimum required	Desirable additional enhancements
[a]2D sections		Orthogonal Sections with translation	Arbitrary orientation, Section rotation, Thick sections >1 pixel, Curved "surface" extraction
Projection geometries		[b]Isometric Pixel shift (limited angles) Rotation or tilt	Arbitrary orientation, Full matrix rotation, Pan & zoom, Combinations (e.g., "fly-by"), With cut-aways
Z-coding	"Focus" animation	Simple *z*-movie	Interactive arbitrary section movie On-the-fly section movie
	Motion parallax	Simple pre-calculated movie	Interactive pre-calculated movie, Motion compression, On-the-fly movie (with interaction)
	Stereo parallax	Manual stereo pairs	Automatic stereo, Stereo with perspective
	"Height" views	Maximum int *z*-coordinate	Threshold *z*-coordinate, *z*-coordinate of high gradient
	Perspective	Orthoscopic	[b]*z*-perspective
Time-coding		*t*-movie	*t*-coordinate
λ-coding		λ-movie 3color channels	λ-coordinate, Arbitrary color channels
Special geometry hardware			OpenGL with enhancement, *z*-buffer hardware "geometry engine"

[a]XY orthogonal sections are the basis of "thru-focus animations." Many systems now permit arbitrary (including "oblique") sections to be extracted from a 3D volume quickly enough to be considered interactive. Curved sections (rarely supported) are particularly useful for cellular structures. They can sometimes by produced by pre-processing using line-segments extracted serially from a 3D stack.
[b]Isometric and *z*-perspective mapping (G) functions increase the perception of depth in static views, and remove the ambiguity of depth seen in some rotating projections.

also around x_v. The following two transforms (around y_i and z_i) are then around oblique (i.e., general) axes in the view space. Our rotation is thus three separate twists around axes: $x_i = (a_x, b_x, c_x)$, followed by $y_i = (a_y, b_y, c_y)$ and then $z_i = (a_z, b_z, c_z)$. The G function, Eq. (2), for each twist is a formidable computation with three subcomponents

$$x_{\text{twist}} = x[a^2 + C(1 - a^2)] + y[ab(1 - C) + Sc] + z[ac(1 - C) - Sb] \qquad (6)$$

$$y_{\text{twist}} = x[ab(1 - C) - Sc] + y[b^2 + C(1 - b^2)] + z[bc(1 - C) \text{ v } Sa]$$

$$z_{\text{twist}} = x[ac(1 - C) - Sb] + y[bc(1 - C) - Sa] + z[a^2 + C(1 - a^2)]$$

where S is the sin(twist angle), C is the cos(twist angle) around an axis (a, b, c), and a is the $\cos\Theta_{\text{twist}}$, b is the $\cos\Phi_{\text{twist}}$, $c = \cos\Psi_{\text{twist}}$, Θ, Φ, and Ψ are the view space polar coordinates of the twist axis (Fig. 14.7).

This whole transform must be repeated for each of the three re-orientation axes $(a, b, c)_x$, $(a, b, c)_y$, and $(a, b, c)_z$. A viewing transform should ideally be added to observe the rotated structure from different viewing positions. However, by fixing the view direction, this additional step is avoided. The efficiency (and ultimately, the speed) of the geometric algorithm is determined by the degree to which the general form (6) can be simplified. If all rotations are specified around the observer's axes (x_v, y_v, z_v) the direction cosines (a, b, c) become either zero or unity. It is also easier for the user to anticipate the final orientation when the rotation axes do not change between each component twist. For a fixed viewing axis along z_v, a tilt θ (around x_v) is obtained by $a, b, c = 1, 0, 0$ giving

$$x_\theta = x_i, y_\theta = y_iC + z_iS, \quad z_\theta = -y_iS + z_iC \qquad (7)$$

where S is sinθ and C is cosθ. When combined with a subsequent φ rotate (around y_v) this becomes

$$x_\varphi = x_\theta C - z_\theta S, \quad y_\varphi = y_\theta, \quad z_\varphi = x_\theta S + z_\theta C \qquad (8)$$

where S is sinθ, C is cosθ, and a final Ψ turn (around z_v) gives

$$x_\Psi = x_\varphi C - y_\varphi S, \; y_\Psi = x_\varphi S - z_\varphi C, \; z_\Psi = z_\varphi \qquad (9)$$

where S is sinφ and C is cosΨ.

The projection will eventually be done in the reoriented view coordinates $V(x_v, y_v) = P(x_\Psi, y_\Psi, z_\Psi)$.

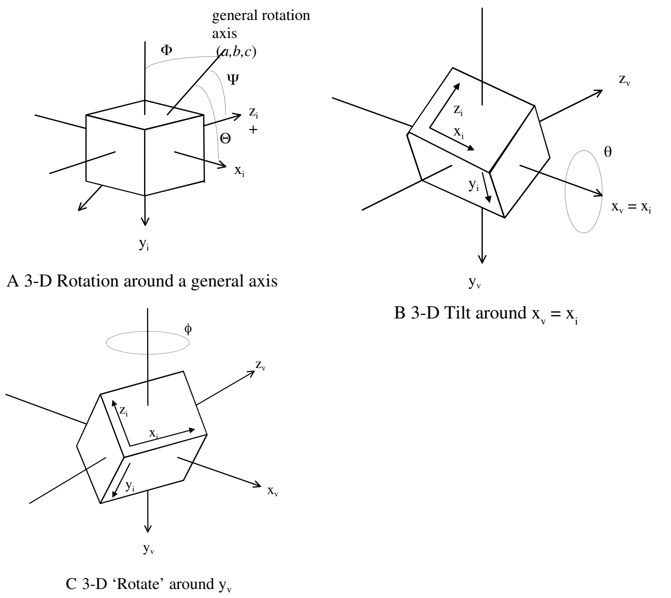
general rotation axis (a,b,c)
Φ
Ψ
Θ
z_i
+
x_i
y_i
A 3-D Rotation around a general axis
z_v
z_i
x_i
y_i
θ
x_v = x_i
y_v
B 3-D Tilt around x_v = x_i
φ
z_v
z_i
x_i
y_i
x_v
y_v
C 3-D 'Rotate' around y_v

FIGURE 14.7. Rotation transformations. 3D rotations can be performed in the image-space around a general axis of rotation (A). General re-orientation requires rotation around three axes x_i, y_i and z_i. A simpler (and thus faster) scheme is to use a "tilt" (B) followed by a "rotate" (C) around x_v and y_v in the view-space. If viewing along z_v, no additional information is obtained by a z_v "turn."

If the twists are "tilt first, followed by rotate" and the viewing axis is oriented along x_v, y_v, or z_v, the twist around that axis can (optionally) be omitted because no more structure will be revealed (Fig. 14.7). By thus omitting the turn (9) and projecting (and viewing) along z_v, the resultant (x_v, y_v, z_v) vectors only change as a function of x_v and z_v (i.e., $dy_v/dx_i = 0$) while traversing a row of image data. This can lead to extremely rapid projection algorithms. The above scheme is used for the 3D visualization routines in Lasersharp, which are executed entirely on the CPU without any involvement of the graphics hardware.

Other tricks can be used to optimize the rendering geometry.

Working in Image or Space View

One implementation approach is to progress through the image space (I space) coordinates (in x_i, y_i, z_i), voxel by voxel, transforming each to view space (V space) coordinates (in x_v, y_v, z_v) before projecting each intensity into the final 2D view at (x_v, y_v). For an image of $nx_i \times ny_i \times nz_i$ voxels, the orthoscopic transformation proceeds via N serial planes or sections of data, normal to z_i in forward (n = 1, nz_i) or reverse (n = nz_i, 1) order. Alternatively the same G function can be implemented in V space. There are now N planes normal to z_v (and thus cut obliquely through the image volume). For each V(x_v, y_v, z_v) the contributing I(x_i, y_i, z_i) are found and the computation can again proceed in forward (n = 1, nz_v) or reverse (n = nz_v, 1) order. The V space implementation makes the G function more difficult but facilitates straightforward projections (P) (Fig. 14.8). The I space implementation is the reverse. The V space method has many more advantages for geometric polygon data than for rastered voxels. Hybrid implementations are also possible, combining both I and V space components. In a hardware-accelerated OpenGl implementation, a favorite approach is to take each image plane (i.e., to progress through I space) and warp it into its projected (rotated) aspect in view space. The warped frame is then mapped onto the view layer by layer. Sophisticated graphics cards have hardware for texture mapping that assists the painting of images onto objects using this technique by altering the view pixels according to the color of the image. This texture mapping hardware can be used to paint the warped frames into the growing view modifying the output by opacity values controlled by the voxel intensities. Hardware texture mapping is used extensively by Volocity and Amira packages.

In all these examples the reconstruction process has resulted in a loss of z_v dimensional information. Some of this may be automatically retained by the P function (discussed below), but an efficient G function can further optimize the dimensional content of the view.

How Do 3D Visualizations Retain the z-Information?

True 3D visualization requires that z_v depth information is retained or at least partially restored when the image is mapped into a 2D view.

Stereoscopic Views

Some impressive methods of coding z_v information use stereoscopic techniques (Tables 14.6 and 14.7; Figs. 14.9 and 14.10). These require that an observer be simultaneously presented with a left-eye and right-eye view differing by a small φ rotation. The author has found the following geometry to give acceptable results: for views of width x, angular difference φ_s, viewed at a distance d with an interoccular spacing D

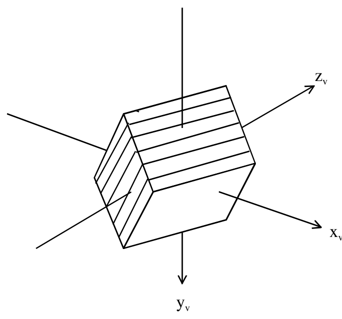

A I-space projection via serial x_iy_i sections

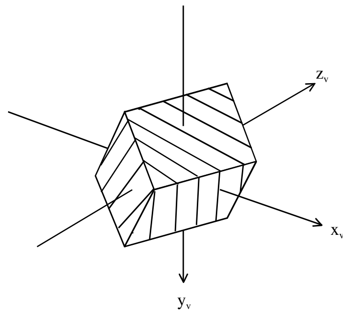

B V-space projection via serial x_vy_v sections

FIGURE 14.8. V- and I-space projections. I-space voxel reconstructions (A) proceed via serial x_i,y_i sections that are oblique to the viewing axis. This is the most efficient way of processing voxels in "object order" and is used by most voxel renderers. V-space algorithms (B) process x_v,y_v sections that are normal to the viewing axis. This z_v-ordered reconstruction is more useful for constructing polygon objects than for voxels.

$$D = 0.05 - 0.07\,\text{m}, \quad d = 0.25 * x/D\ \text{m}, \quad \varphi_s = 2 * \arctan[(0.5 * D/d)] \tag{10}$$

for example, if D = 0.06, x = 0.06, then d = 0.25 and φ_s = 13.6°.

A simpler alternative to the computationally intensive rotations is to shift each section horizontally (in x_v) by a constant factor of the z_v coordinate during a top-down compositing projection (3). This corresponds to a stereo pixel-shift G function

$$x_v = x_i + \delta x * z_v, \qquad y_v = y_i, \qquad z_v = z_i \tag{11}$$

where $\delta x_{left} = \tan(0.5*\varphi_s)$ and $\delta x_{right} = -\delta x_{left}$.

From Eq. (11) and the viewing conditions of Eq. (10), δx is ± tan (7.8°) or about 0.14 times the z-spacing (Fig. 14.9). A slightly different equation is described by Cheng and colleagues (1992) and its derivation is attributed to Hudson and Makin (1970). It can be used to derive an optimal pixel-shift. Using a notation consistent with the above

$$\delta p = 2*nz_{calib} * M * \sin(\arctan(\delta x * nz_i/nz_{calib}) \tag{12}$$

where δp is the parallax shift between equivalent points in two views (ideally kept around 3–5 mm); nz_{calib} is the the calibrated z-size of the data (thickness of the original specimen), and M is the magnification.

The pixel-shift method is only an approximation. In particular, the result is stretched out or warped in the x-direction by a small

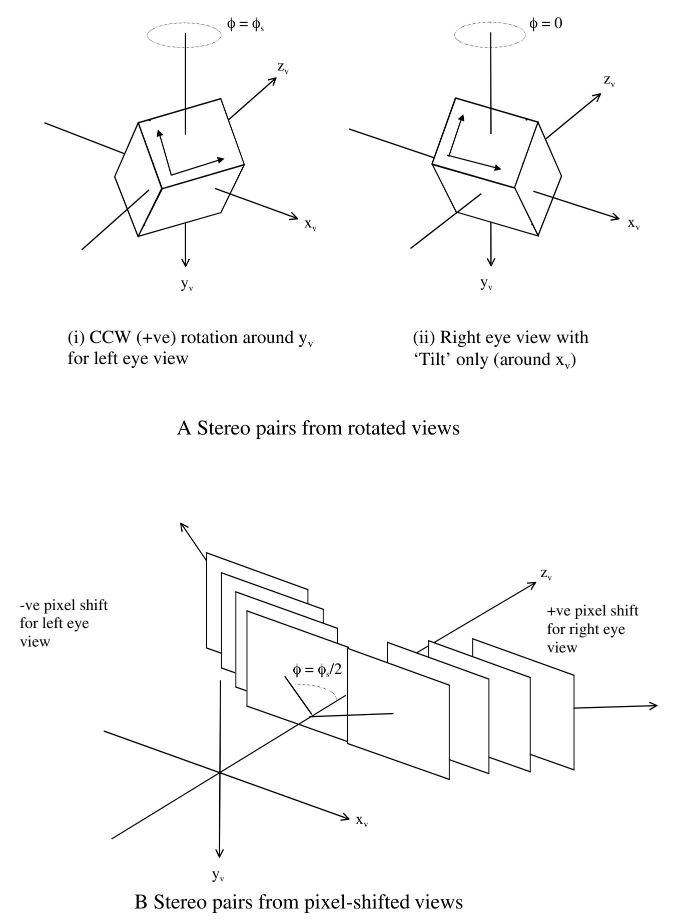
φ = φs
zv
xv
yv
φ = 0
zv
xv
yv
(i) CCW (+ve) rotation around yv for left eye view
(ii) Right eye view with 'Tilt' only (around xv)
A Stereo pairs from rotated views
-ve pixel shift for left eye view
+ve pixel shift for right eye view
zv
φ = φs/2
xv
yv
B Stereo pairs from pixel-shifted views

FIGURE 14.9. Pixel-shift and rotation stereo. Pairs of views differing by typically around ±7–8 deg (depending on pixel dimensions and inter-plane spacing) of y_v rotation ϕ_s (A) can be extracted from a sequence and displayed using anaglyph, switched-view or other stereo viewers (see text). The pixel-shift approximation to these rotations (B) results in only trivial distortion and is much faster to implement for small angles about the z_v axis. See Figures 14.5 and 14.10 for example images and the section on 3D depth information for details of stereo generation algorithms.

factor of $1/\cos(0.5 * \varphi_s)$, but for small angles this can be neglected. This shearing and warping algorithm is the basis for fast texture-mapped voxel projections (e.g., Cabral *et al.*, 1994; Lacroute and Levoy, 1994; Elisa *et al.*, 2000).

The two views, or stereo-pair, must be fused into a 3D representation by positioning each in the display space so as to occupy the entire field of view (or at least the central region) for each corresponding eye. The observer then perceives the combined information as a single 3D view located near the viewing distance d, depending on the origin of the z_i-coordinates used in the above equation. For z_i-coordinates centered in the middle of the image volume, the view depth is centered about d. A few high-contrast features must be present in the field in order to successfully fuse the reconstruction. This makes the choice of algorithm and associated parameters critical for successful stereo presentations. The stereo scene geometry is efficiently accomplished by placing the views in two halves of a display, bisected in *x* or *y*, and using a viewing aid. The viewer must make the two views appear to be coming from the center of the field while keeping the observer's ocular convergence/divergence near to parallel (i.e., relaxed as though viewing at a distance). By carefully editing a vertical sub-region (e.g., 384 × 512 pixels) of interest, side-by-side pairs can be viewed in full color on a horizontal display format (e.g., 768 × 512, 1024 × 768, etc.) without subsampling. Side-by-side stereo-pairs are easily viewed with horizontal prismatic viewers. An alternative is to fix one's binocular convergence point at infinity and refocus each eye onto the respective view (using the lens and cornea only). The left and right views may also be swapped and the eyes crossed or converged to a point between the observer and screen. Some seasoned stereoscopists can fuse stereo-pairs using these methods without additional aids, although prolonged viewing can give rise to eye strain and headaches. Above-and-below pairs can be seen through vertical prismatic viewers, but this geometry cannot be so easily fused by the unaided observer!

Partitioning the color space into two distinct regions allows full size anaglyph stereo-pairs to be observed in monochrome (gray levels only). Both views occupy the entire pixel display area and are transmitted to the corresponding eyes by RG or RB spectacles. Due to the spectral characteristics of some monitor phosphors and the availability of low-cost filter materials, some bleed-through of signal between RG channels often occurs. Red/cyan viewers often have improved extinction. The optimal intensity balance between the component views must be individually determined. Anaglyph stereo-pairs can be fused by observers irrespective of their capacity to differentiate colors. Even rare red/green color blindness is no obstacle provided sufficient intensity levels can be differentiated, although it is usually found that around 10% of observers fail to perceive 3D effects from stereo cues alone (Richards, 1970). Because the anaglyph views occupy the same physical area, the eyes are drawn into a convergence naturally. The monitor should be as large as possible to increase the distance from the viewer and decrease eye strain, that is, so the convergence angle is as small as possible but each eye is focused at a distance. Health and safety recommendations usually specify at least 18″ comfortable viewing distance for VDUs (more for extended viewing) with alternative work breaks every hour.

In order to maximize simultaneously spatial and color resolution, the temporal display space can be partitioned to display the component stereo-pairs. This requires more sophisticated hardware than the previous methods at increased cost. The left and right component views are displayed alternately on the video monitor in rapid succession. Observers watch through a viewing device that synchronously blanks and unblanks the visual field of each eye while each corresponding view is displayed. These alternate (or switched) display stereo systems are characterized by differences in the format of the video signal, the switched viewing hardware, and the method of synchronization. Older video stereo systems display images in two alternate and interlaced **fields** of each video **frame**. This method gives half the temporal and *y*-axis resolution of a normal video signal, an obtrusive (25/30 Hz) display flicker, as well as the low intensity associated with interlaced displays. Computer displays are exclusively non-interlaced but alternative frames may be used to show stereo components rapidly in succession. An interlaced implementation will require the two component images to be interleaved line-by-line in the display memory. A more convenient organization is to have sequential buffers for the two fields which can be updated independently. Non-interlaced computer displays give a brighter view with a flicker-free refresh rate of 60 to 90 Hz. This would allow alternate frame non-interlaced stereo, but would still exhibit noticeable flickering around 30 to 45 Hz. A continuous stereo display requires at least 120 Hz and preferably a double-speed scan of 180 Hz.

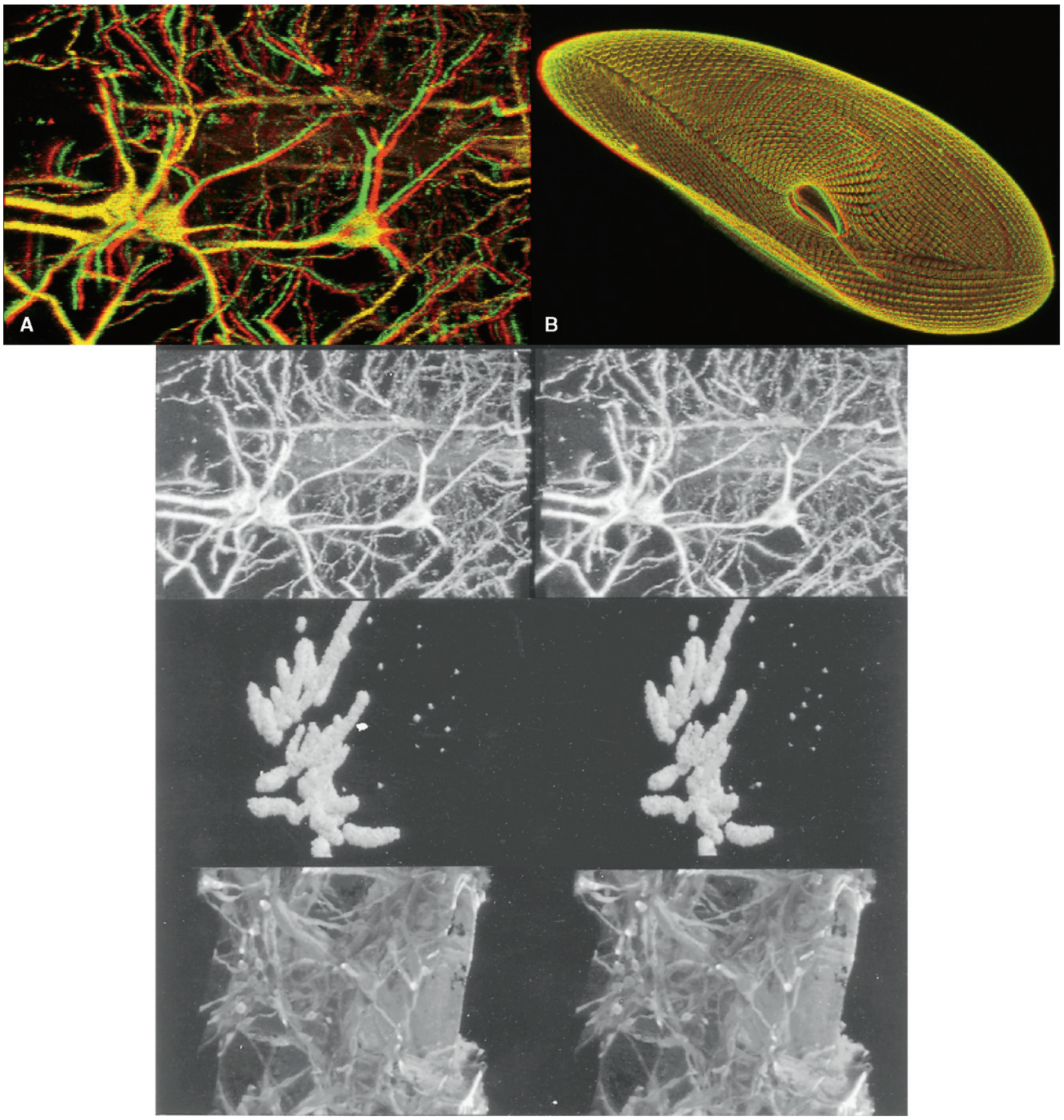

FIGURE 14.10. Example stereo images. (A) Anaglyph (two color, red/green) stereo-pair of Golgi-stained nerve cells, generated by the pixel-shift method (see text). The alternative method of extracting two images from a rotation series [shown immediately below (A) as a side-by-side pair] produces a virtually identical result to (A) for small angles about the z-axis. (B) Anaglyph stereo-pair of fluorescent Paramecium. [Data for (A) and (B) courtesy of Bio-Rad Microscience.] The third pair of panels shows a stereo-pair of voxel-rendered images representing Feulgen-stained chromosomes from the plant *Milium.* (Original data from Bennet *et al.,* 1990.) Voxel gradient lighting is used with a high-opacity α-blend algorithm to give an effect of "solid" structure. The final panels show a triple-stained thick section of skin showing extra cellular matrix proteins and vascular structures. Simple maximum projections of each channel z-series are combined into the 24-bit RGB view. While the anaglyph stereos can span the entire display window but require the color space for the stereo effect, these full color side-by-side stereo pairs (as for monochrome pairs) can span only half the available display resolution. These alternative stereo display methods illustrate the way that display resources can be "traded" for improved (x,y) resolution, z-depth or multi-channel (color) rendition. Side-by-side pairs in this figure should be viewed by divergent eyes or viewing aids (i.e., with eyes relaxed as when viewing distant objects but focused on the page). This is best achieved by focusing on a distant object and bringing the page into view while keeping the eyes relaxed but refocused on the page. If the eyes are crossed or a convergent viewing aid is used, the 3-D effect will appear "back-to-front." This can be problematic with some maximum projections (e.g., the Golgi-stained neurons above) where some brightest features are towards the "back" of the rotated object in some views. This is often found when there is attenuation with depth in the sample. Maximum intensity can incorrectly bring these features to the "front" of the view. Samples with more isotropic intensity distributions with depth (e.g., the skin images above) tend not to show these anomalies.

Some high-resolution stereo displays still use an interlaced storage mode (at half the y-resolution) for stereo presentation. All video display systems suffer to some extent from flicker arising from an interference with mains-powered room lights and should be run in reduced ambient lighting.

Synchronizing the display to the switched viewing system can be accomplished in a number of ways. A bright intensity marker in each video frame can identify the left and right views, and this has been used to trigger a photo switch placed over the corner of the video monitor. This switch controls synchronous LCD shuttered viewers. The synchronizing pulse can be generated directly from the field or frame synch of the display signal and passed to the viewers by cable or optical (infra-red) link. A more convenient alternative to switched viewers is the polarizing LCD shuttered screen. This is a large LCD shutter (often constructed from two parallel units for faster switching) that toggles between two polarization states. The left- and right-eye views are thus differently polarized and can be viewed through inexpensive glasses. Plane-polarized shutters (and glasses) give the best extinction, but clockwise and counterclockwise rotary polarization allows for more latitude in the orientation of the observer's head (important when a large group is viewing a single monitor!). Example stereo views are shown in Figure 14.10 (and also Figs. 14.5 and 14.24). The Imaris package has a number of selectable stereo modes depending on the type of viewers to be used (these include Raw Stereo — using the OpenGL functions, alternate image (interlaced modes), and three combinations of two-color anaglyphs). The 3D-constructor plug-in for ImagePro Plus (Media Cybernetics Inc.) also supports OpenGL stereo.

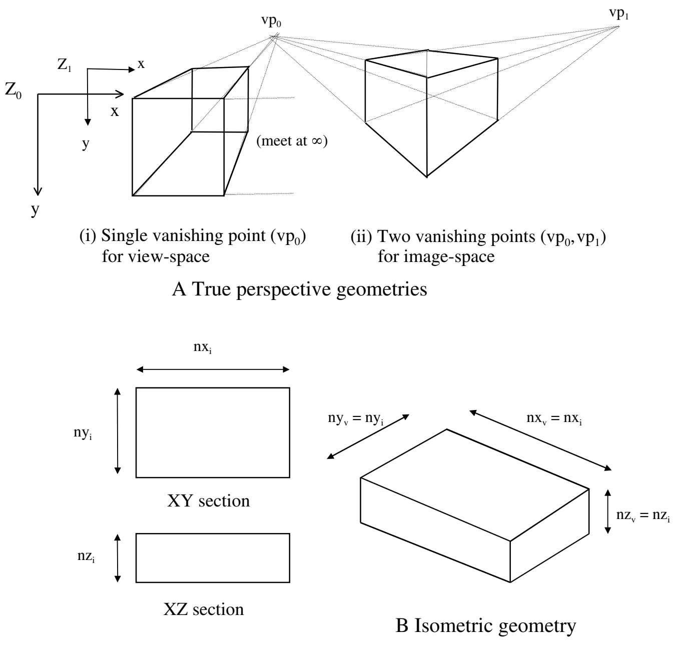
vp0
vp1
Z1
x
Z0
x
y
y
(meet at ∞)
(i) Single vanishing point (vp0) for view-space
(ii) Two vanishing points (vp0,vp1) for image-space
A True perspective geometries
nxi
nyi
XY section
nzi
XZ section
nyv = nyi
nxv = nxi
nzv = nzi
B Isometric geometry

FIGURE 14.11. Non-orthosopic views. True perspective views (A) give the most "realistic" reconstruction geometries. A simple approximation can be implemented in the view-space (1) with one "vanishing point." x_v, y_v coordinates are reduced by a linear function of z_v between z_0 and z_1(see text). A general perspective G-function for image-space implementation (2) with rotation around y_v requires two vanishing points. Isometric reconstructions (B) retain the physical dimensions of the original image axes (rather than the trigonometrically projected axis lengths). 3D distance measurements can thus be made directly on the views.

Non-Orthoscopic Views

Visual perception of depth makes extensive use of non-stereoscopic cues, and these can be coded by appropriate algorithms into a corresponding part of the display space. A series of G functions exist that code depth information with unmodified intensities. These are the non-orthoscopic transformations and include both perspective and non-perspective geometries (Fig. 14.11). The most straightforward of these algorithms require that the corresponding view coordinates for each data voxel are modified by the image z-coordinates. The **isometric** G function involves a constant shift in screen x_v and/or y_v coordinates as the I space renderer traverses each dimension of the data

$$x_v = x_i + x_i\cos\Psi, \quad y_v = y_i + y_i\sin\Psi + z_i, \\ z_v = z_i \quad \text{and usually } \Psi = 60° \qquad \textbf{(13)}$$

This geometry (as the name suggests) gives rotated x_v, y_v and z_v, axes in the same proportions as the original image axes (for rendered examples, see Wilson, 1990). Direct x_i, y_i, z_i measurements can be made from the 2D view screen.

True **perspective** views attempt to visualize the data as a large real-world or macroscopic object with x_v and y_v converging to a vanishing point at a large z_v distance. This point is on the horizon (usually in the center of the field). The perspective G function decreases the dimensions as a linear factor of the z-coordinate. So after the data have been rotated, the projection is accomplished through a new perspective space (x_p, y_p). True perspective can be approximated in the G function by

$$z_p = z_\Psi, \quad x_p = \mathbf{a}x_\Psi/z_\Psi, \quad y_p = \mathbf{a}y_\Psi/z_\Psi \qquad \textbf{(14)}$$

where **a** is a factor reflecting the object-to-observer distance.

Perspective views can be readily interpreted from objects with well-defined structures. This is because we assume such views arise from connected features such as real-world surfaces and edges. Popular optical illusions indicate this is not always true! Connectivity between neighboring voxels in a confocal laser scanning microscopy (CLSM) fluorescence image can rarely be assumed without substantial *a priori* knowledge and then only after careful control of noise. Non-orthoscopic depth coding is useful for removing ambiguity from stereoscopic views. Volocity and Imaris produce both orthoscopic and perspective 3D (and 4D) views.

Temporal Coding and *z* Depth

Time axes can often be treated in exactly the same manner as depth or z-coordinates. This is a useful observation because many visualization packages do not specifically recognize time points. Thus t-coordinates can be directly mapped by animation, coded in the intensity or color space, and even represented in non-orthoscopic or stereoscopic views. The importance of time points as a component sampling space in 4D imaging is encapsulated within the so-called 4D tixel object. Significant efforts have been invested in the efficient visualization of tixel images within the 5D display space (Kriete and Pepping, 1992). z-Position can be inferred from the display temporal space by animating serial sections as a through-focus sequence or by motion parallax (Fig. 14.12) from a rotation series (Wallen *et al.*, 1992). Since xy-acuity improves smooth motion perception, large rotated views require reduced angular increments as well as higher refresh and framing rates compared to those from smaller volumes.

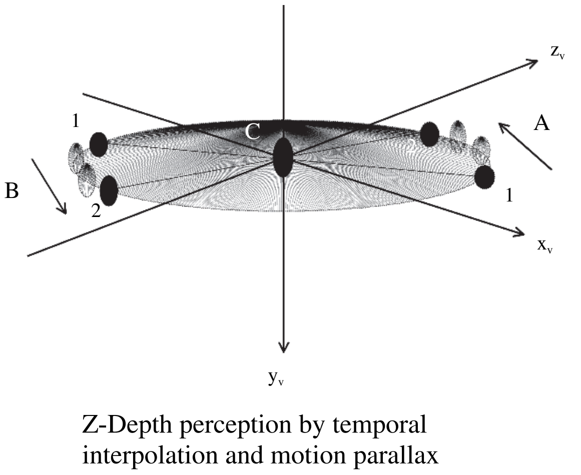

z_v
A
1
C
1
B
2
x_v
y_v
Z-Depth perception by temporal interpolation and motion parallax

FIGURE 14.12. *Z*-depth by temporal interpolation and motion parallax. If a similar feature is seen in two sequential views of a rotation series viewed along z_v (e.g., the dark shape appearing at "1" in the first view and at "2" in the second), two processes contribute to the perception of its depth within the view. (1) The direction of motion, either left or right across the field of view will determine whether it is perceived to be behind (A), the center (C), or in front (B) of the screen. (2) provided the views are at small angles apart and shown in a "smooth" sequence (which may need up to 18 fps), the details are mentally interpolated in time (taking into account the perceived motion) to "fill in" the missing information (dotted features). For a fully transparent view with no other depth cues, front and back may be arbitrarily reversed by different observers.

Mapping the Data Values into the Display

As with the G function, data values must also be transformed to the display by a well-defined operation. This is the combination, compositing or projection function P, described in Figure 14.6 (examples in Table 14.8 and Fig. 14.14).

The Visualization Model

It is useful to consider even the simplest P function in terms of a lighting model. In a gross simplification, each image voxel is considered to have a brightness equivalent to the amount of light emanating from a corresponding point in the specimen and collected by the microscope objective. Digital processing to more closely realize this goal for CLSM imaging requires a knowledge of the microscope transfer function (e.g., Sheppard and Gu, 1992, 1993) and the use of digital restoration methods (e.g., Holmes and Liu, 1992; Shaw and Rawlins, 1991; see also Chapters 23 and 24, *this volume*). For now, the 3D image is considered as the physical or macroscsopic object, itself being imaged, as if by a lens or eye, to a 2D view. Light rays from each point voxel in the image would contribute to an equivalent (but not unique) point in that view. This mapping of object points × image voxels × display view pixels is the crude model. This is refined and made more elaborate by (1) segmenting the multi-dimensional image data into a set of objects, (2) considering other objects in the path of each simulated light ray, and (3) adding additional, artificial lighting and surface effects. These aims are met using physical or material properties attached to the objects.

Choosing the Data Objects

So far, we have considered the image as an array of voxel (3D) or tixel (4D *x*, *y*, *z*, t) objects with no implied connectivity. Computer-aided macroscopic imaging and display systems have fostered the growth of visualization models based on the grouping of voxel samples into geometric objects. The consequence is a growth in special hardware and software for efficient treatment of vectorized geometries. Microscope systems invariably produce rastered image arrays. The array dimensions (n*x*, n*y*, n*z*, etc.) imply the arrangement of rows, columns, sections, etc. Vector objects are non-ordered lists of geometric figures, each of which is defined by a very few parameters. Thus, a simple voxel might be five values (*x*, *y*, *z*, intensity, opacity, etc.) but a triangle comprising many tens or hundreds of voxels may be specified with only 10 to 15 parameters (three sets of coordinates plus some material properties). If the material properties vary across the polygon, values at each vertex only need be stored. Each vectoral component will need at least 16-bit integer precision and preferably floating-point. A compact form is to store all vertices in one list or table. Each geometric object is then a set of polygons, specified by indices pointing into the vertex table.

While early workstation programs stored voxels as vectors, the availability of optimized hardware and software for G functions and 3D rendering of rastered byte images has assisted the devel-

TABLE 14.8. Overview of Image-to-View Data Mapping (Projection) Options for Visualizing Multi-Dimensional Biological Microscopy Data

Feature	Parameter	Minimum required	Desirable additional enhancements
[a]Data objects	types	Voxels	n-D array of voxels, Object list, Surface (triangles), Surface (polygon net) Objects "embedded" within voxels
	storage	3D rastered array	n-D rastered array, object vector list
Selective enhancement of features		Basic filters, Volume cut-away Region of interest/edit, Intensity segment, Color channels	Gradient segmentation, Image masking, Opacity/transparency Material properties, Morphological filters, "Seed/flood fill" Object modelling
[b]Projection algorithms		Maximum Average	Front, Z-co-ordinate, α-blend, SFP, Iso-intensity surface, "Local" projection
[c]Special graphics resources		VGA graphics	OpenGL with acceleration, Texture mapping, Hardware shading/lighting etc., α-buffer

[a] Data objects are usually voxels or lists of vertices defining geometric surfaces. Other surface descriptions are possible. AVS allows for a particularly large range of geometries, while in most object reconstructions, the options are usually restricted to triangulated surfaces — primarily to make use of efficient accelerations in the graphics system.
[b] Some geometric object renderers use Front or α-blend P-functions in the same way as for voxel objects. Specific "surface" algorithms may also be implemented that capitalize on the connectivity of the geometries. There is always a trade-off between the portability of a program across platforms (or over new versions of platforms) and the use of non-standard "special" hardware. The OpenGL standard largely avoids these problems by setting the interface requirements and providing standard support for new hardware. SFP = simulated fluorescence process.

opment of voxel visualization algorithms. The most efficient way to process rastered voxels is by whole-image operations. I space implementations effectively warp successive orthogonal (xy, xz, or $tz)_i$ sections, using a transformation geometry engine, to their projected shape in the final view. Rows and columns of data are traversed in forward or reverse order to preserve the forwards or backwards compositing direction. The only drawback of this method, as opposed to a z-ordered list of polygons, is the throughput to the display. Because the entire image data must be streamed into the display, bandwidth is critical. This requires highly efficient pipelined operations to achieve a display rate sufficient to service the output from an optimized geometry engine. The highest specification systems use multiple display devices (often video projectors) to simultaneously render multiple views for immersive reality installations. So-called multi-pipe versions of these visualization programs are used to massively increase the data throughput to the display. The vectoral representation is more efficient for triangles encompassing more than about 20 equivalent voxels, provided the segmentation algorithm is justified for the particular data. Computer models allow entire surfaces and bounded volumes to be described by single parametric equations using, for example, Bezier coefficients (see Watt, 1989). This type of simple object definition is generally not practical for confocal fluorescence data due to the low signal-to-noise and discontinuities in antibody or other stains. As a result, many vertices must be individually stored.

Vectored object lists can be traversed in I or V space in object order. Thus, complex figures can be rotated and projected individually. Refinements in geometric object technologies may appear to place voxel rendering at a disadvantage due to its ordered processing of many more data points. Choice of data objects is largely determined by the amount of information known about the specimen, the sophistication or realism required in each view and the availability of appropriate hardware and software on the chosen platform. It should now be apparent that there is no fundamental distinction between any of the data objects discussed. A trade-off between processing speed and transfer rate must be weighed against the problems or bias associated with segmentation of the image data into parametric structures. In any case, voxel rendering speeds are now equivalent to the speed at which vector graphics objects could be drawn just a few years ago. All of the compositing or P function rules described below can be applied to any data objects.

Sophisticated graphics systems are now relatively inexpensive and are supplied with even modest-specification PCs. Some include hardware accelerated geometry-processing engines, with standardized OpenGl interfaces, intimately linked with the GPU and display memory together with additional buffers, LUTs, etc. Thus many of the above operations are now readily available to any software developer writing for a standard hardware platform.

Segmenting the Data Objects

Segmentation is a process by which objects are extracted from the rastered voxel image data. Voxels are selected according to their brightness and/or by some property linking them to other voxels. A lower and/or upper threshold may be applied producing a segmented band containing all the voxels of a particular object. Most systems allow this intensity segmentation to remove background or to isolate a homogeneously stained structure. Threshold values are readily chosen by masking a histogram and observing this simultaneously with an interactive, color-banded screen display of the segmented voxels. Histogram peaks indicate subpopulations of background voxels, possible structural features, etc. This edited histogram produces a photometric look-up table (P-LUT) through which the image is rapidly mapped. Morphological segmentation requires a selection based on some connectivity rule such as the geometric surface objects extracted by the Marching Cubes (c.f. VoxBlast) or Delaunay Triangulation (c.f. Visilog) algorithms. Three-dimensional intensity gradient filters can also find or enhance boundaries between geometric objects. Cheng and coworkers describe the use of such a filter to extract a gradient image, which is then blended with the original to enhance edges. Using the earlier notation

$$\mathrm{I}_{\mathrm{out}}(x_i, y_i, z_i,) = \mathrm{I}_{\mathrm{in}}(x_i, y_i, z_i,)\ [\mathrm{k} + (1 - \mathrm{k})\ \mathrm{grad}(\arctan(\mathrm{I}_{\mathrm{in}}(x_i, y_i, z_i,))] \tag{15}$$

where the arctan is an (optional) approximation to a sigmoidal background suppressor and grad is the unsigned 3D gradient

$$\mathrm{grad}(x_i, y_i, z_i)\ \grave{}= |[(d\mathrm{I}/dx_i)^2 + (d\mathrm{I}/dy_i)^2 + (d\mathrm{I}/dz_i)^2]$$

This 3D gradient is simply the resultant of the unsigned component gradients along each axis. These individual components are conveniently approximated (for low noise data) by subtracting the values on each side of the voxel whose gradient is required, that is, $\mathrm{grad} = (|((\mathrm{I}(x_i + 1, y_i, z_i) - \mathrm{I}(x_i - 1, y_i, z_i))^2 + (\mathrm{I}(x_i, y_i + 1, z_i) - \mathrm{I}(x_i, y_i - 1, z_i))^2 + (\mathrm{I}(x_i, y_i, z_i + 1) - \mathrm{I}(x_i, y_i, z_i - 1))^2))/2$.

Gradient filters are also extensively used to provide data for the realistic artificial lighting effects (discussed later). Other background filters are based on patch convolutions with kernel weights given by smoothing functions. Forsgren and colleagues (1990) use a 3D Gaussian filter where the mask weights are given by:

$$\mathrm{F}(x, y, z) = 1/(\sigma^3 2\pi|(2\pi))\ \exp\ (-\ (x^2 + y^2 + z^2\ )/\sigma^2) \tag{16}$$

different strengths are specified by the width term σ. This filter is separable and is readily implemented as a sequence of 1D filters, allowing for asymmetric sampling in the multi-dimensional image. A general approach is to use a 3D filter (or ideally a PSF deconvolution) with a cut-off at the Nyquist frequency (see also Chapters 4 and 25, *this volume*), followed by a threshold segmentation of the filtered output. The segmented output is then used in a logical test (or mask) to segment the original image. Segmentation (Fig. 14.13) may simply exclude background voxels or the included voxels can then be grouped into polygon objects. Voxel objects can use a material look-up table (M-LUT) for each property. It is possible to specify all material properties for any object types as indices in one or more material look-up tables (M-LUTs) and to use these to separate different materials within the volume. The Analyze package has a good example of a dedicated segmentation menu that brings together image edit, morphology operations, and object/surface extraction functions. The Surpass optional module in Imaris groups together the object segmentation capabilities of that package.

Scan Conversion

After geometric rotation, etc., the data objects are drawn into the final view. For polygons, surface nets, etc., this requires a scan conversion whereby the vectors are turned into rastered lines of pixels (Watt, 1989). A pixel view of each polygon patch is then composited into the final view as for rastered voxels. A simple approach is to draw a closed outline and to use a fast-fill algorithm, modified by any shading required. It is often more efficient to generate just the ends of each scan line through the polygon, filling the gaps by simple line drawing. For two vertices $\mathrm{S}(x_s, y_s)$ and $\mathrm{E}(x_e, y_e)$ defining the start and end of a polygon edge, there are $(y_e - y_s)$ intermediate scan lines. The view coordinates for the start of the jth scan line are

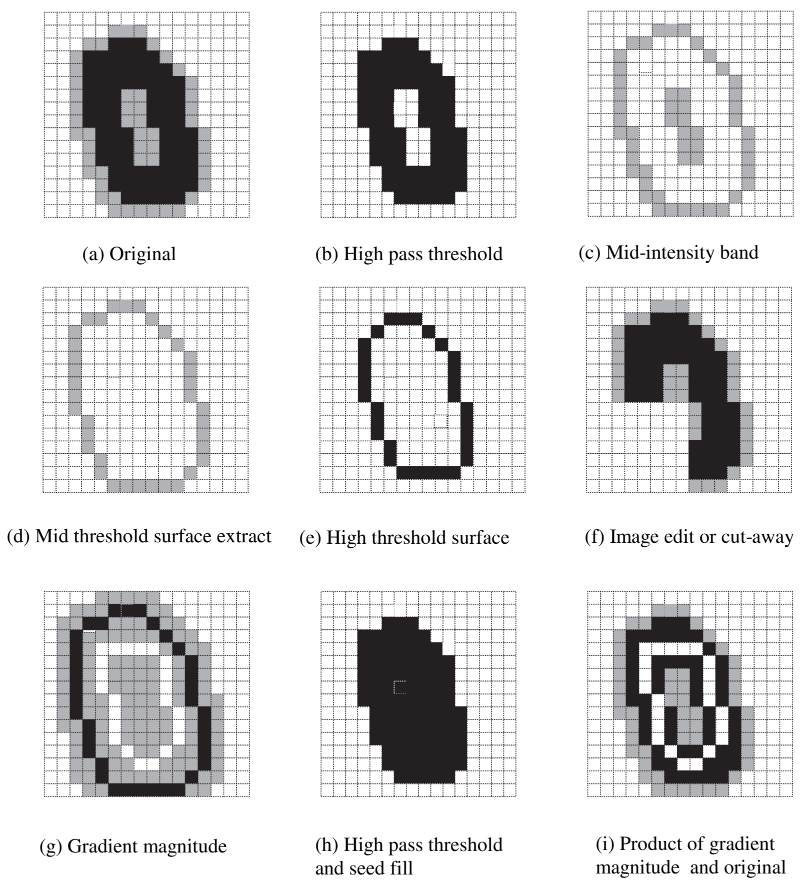
(a) Original
(b) High pass threshold
(c) Mid-intensity band
(d) Mid threshold surface extract
(e) High threshold surface
(f) Image edit or cut-away
(g) Gradient magnitude
(h) High pass threshold and seed fill
(i) Product of gradient magnitude and original

FIGURE 14.13. Object segmentation. Voxels may be segmented from the image volume only to remove background and unwanted features, or they may additionally be grouped into larger geometric objects. (A–I) show 2D slices from a small 3D volume before and after segmenting with various algorithms. High-pass (B) and mid-intensity band (C) are the simplest operations and are often used on their own, or in conjunction with other operators. Surface extractions (D,E) (e.g., Marching cubes, c.f. VoxBlast or Delaughney Triangulation, c.f. Visilog) produce bounded structures obscuring internal details. Manual or semi-automatic image editing or reconstruction cut-aways (F) reveal internal details without corrupting the data values. Gradient magnitude filters (G) highlight voxel boundaries and edges. Thresholded seed fill (H) (c.f. Visilog, ImageSpace) gives a solid object for simple volume estimates, etc. Complex modes such as the gradient magnitude blended with the image (I) (see text) can give reasonable enhancement of edges without artifactual "halos" (c.f. Prism II/DeltaVision).

$$x_v = (\text{int})(x_s + j\delta x), \quad y_v = y_s + j \tag{17}$$

where $\delta x = (x_e - x_s)/(y_e - y_s)$. The ends of each scan line are obtained by a similar calculation.

Scan conversion or rasterization is a well-defined component of the OpenGL graphics pipeline and this affords a convenient point in the reconstruction process to combine or embed graphical objects into a voxel or previously generated pixel view. This is a powerful technique used to good effect by the major rendering packages to show high contrast segmented objects within the context of a general volume view (Amira, for example, allows for an arbitrary number of datasets, image modalities and/or visualization modes within the same display view).

Projection Rules

As each geometric object or image plane is composited into the view, incoming data either replaces or is blended with the accumulating result. The algorithm used is usually a function of the *z*-coordinate, the intensity value, and the associated material properties (Table 14.8). This P function has two components: an arithmetic or compositing (C) function (which may be just a simple assignment) and an optional logical test (T). For the *n*th (of N) frames or objects composited into the view V, a general form is

$$\text{if } \{T\,[I(x_v, y_v, z_v)_n, V(x_v, y_v, z_v)_{n-1}]\} \text{ then } V(x_v, y_v)_n = C\,[V(x_v, y_v, z_v)_n, I(x_v, y_v, z_v)_n] \tag{18}$$

Simple compositing functions (Fig. 14.14) include:

- **Maximum Intensity**

$$\text{if } [I(x_v, y_v, z_v)_n \geq V(x_v, y_v, z_v)_{n-1}] \text{ then } V(x_v, y_v)_n = I(x_v, y_v, z_v)_n \tag{19}$$

Maximum intensity projection, or MIP (e.g., Sakas *et al.*, 1995), is now the most widely used quick visualization function (e.g., see Analyze, Cedara, Imaris, FIRender, Voxblast etc) and can be efficiently implemented as a stand-alone mode or in combination with other algorithms.

- **Average Intensity**

$$(\text{no test})\ V(x_v, y_v)_n = V(x_v, y_v, z_v)_n + I(x_v, y_v, z_v)_n/N \tag{20}$$

Less common than MIP, mean intensity is found in the LSM programs and Analyze. It is useful when the data volume is very dense, which would tend to give a very saturated view with MIP. Because it effectively averages along the projected ray, this function reduces noise but produces lower contrast. This can be partly overcome with an appropriate display LUT.

- **First or Front Intensity ≥ t**

$$\text{if } \{[I(x_v, y_v, z_v)_n > t]\ \&\ [(z_{v,n-1}) < (z_{v,n})]\} \text{ then } V(x_v, y_v)_n = I(x_v, y_v, z_v)_n \tag{21}$$

This is a quick way of exploring a surface or boundary in a voxel representation, particularly as an aid to determining parameters for more complex modes (e.g., see Lasersharp projection modes).

- **Alpha Blend**

$$(\text{no test})\ V(x_v, y_v)_n = (1-\alpha)\,V(x_v, y_v, z_v)_{n-1} + (\alpha)\,I(x_v, y_v, z_v)_n \tag{22}$$

This is the standard mode used for object visualization and works particularly well for voxel objects and is implemented in virtually

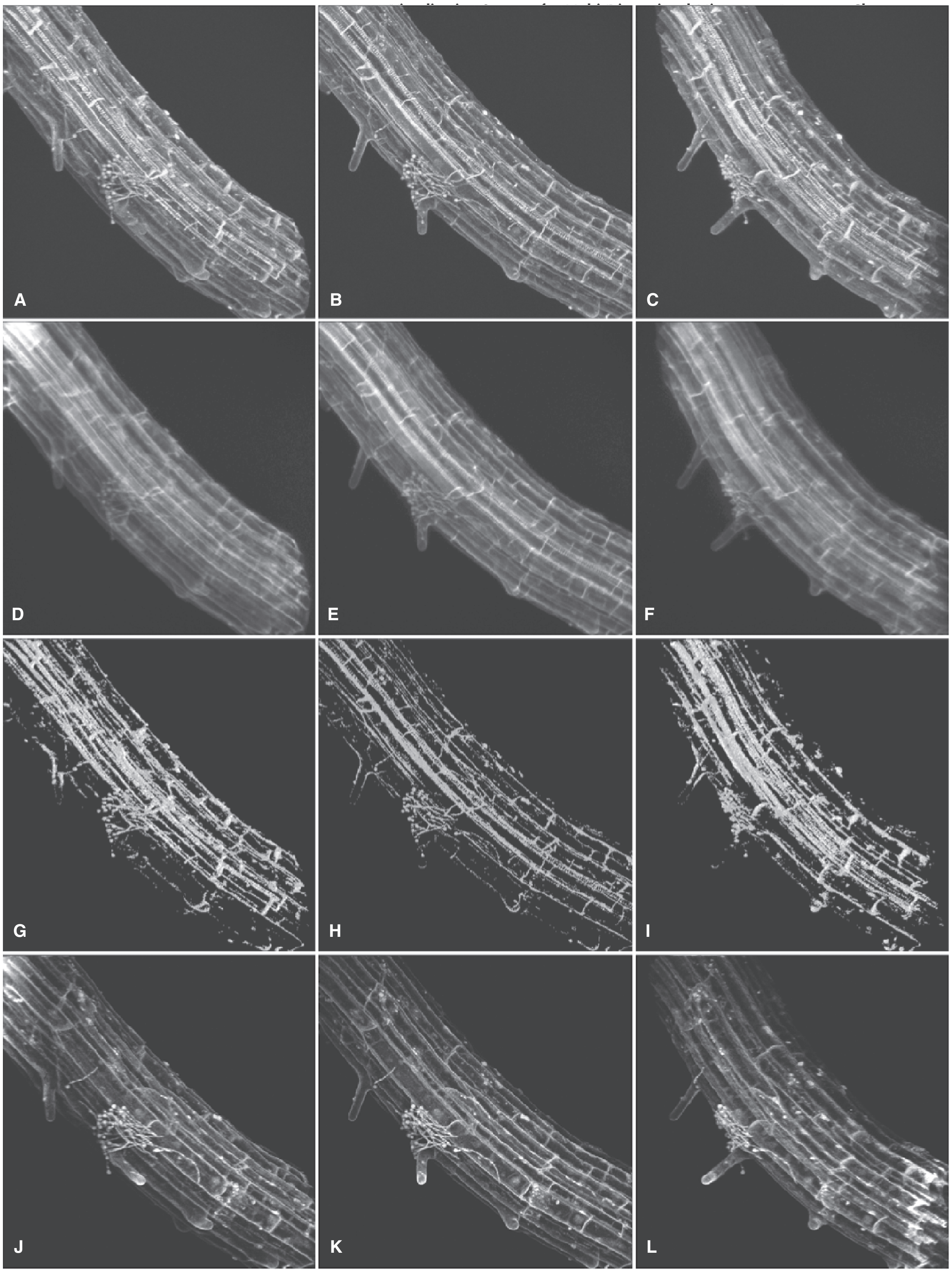

FIGURE 14.14. Projection combination or compositing rules. 3D visualizations of a stack of 130 confocal optical sections through a portion of *Arabidopsis* plant root using Lasersharp (A–C) and Imaris (J–L). Autofluorescence (and a little non-specific fluorescent thiol-staining) shows vascular tissue, cell walls and nuclei and lateral root buds. A small attached fungus is seen attacking the plant along the lower edge towards the center of this portion of root. (Maximum intensity projections as rotations at −30 deg (A), 0 deg (B) and +30 deg (C). Equivalent average projections (D–F) show the characteristic "fuzzy X-ray" character of images made with this algorithm. The first voxel (nearest the viewer) along each cast ray is recorded in (G–I) showing a more solid appearance while retaining original intensity values but at the expense of losing many details. α-rendering at the same angles (J–L) clearly represents the density of the structure as well as fine details but introduces some spurious high intensities where the structure is thin (e.g., at the end of the lateral root tips).

all of the packages in Table 14.1. Although the added complexity of having to set the α parameter sometimes makes it harder to use than MIP for LSM fluorescence data, this parameter is the basis for all opacity/transparency effects (see below).

The tests in Eqs. 19 and 21 may be reversed to obtain minimum and below-threshold versions. The alpha term is a general function that can partly define the physical properties of the rendered object. This blending factor can be dynamically modified as a function of z_v or n during the projection. A Kalman version of Eq. 20 may be implemented in this way; the number of composited frames N need not be known in advance, and the process can be stopped when the required result is reached.

- **Kalman Average**

$$V(x_v, y_v)_n = (1 - 1/n) V(x_v, y_v, z_v)_{n-1} + (1/n)I(x_v, y_v, z_v)_n \tag{23}$$

This is a dynamically modified $\alpha = 1/n$, and the projection may proceed in positive or negative z_v order. These define the front-to-back and back-to-front view space rendering geometries. It should be readily obvious that these two processes afford a simple means of modeling the lighting of voxels from front-to-back or the emission of light from voxels running from back-to-front with respect to the viewer. The latter rendering order also shows the view building up towards the viewer that can reveal internal details of an object during the visualization process, provided the screen is updated during the computation. A display equipped with α-plane hardware (with associated firmware or software) automatically blends the incoming data using factors stored and updated in an alpha memory plane. α-blending may also be implemented entirely in software. This is a standard OpenGL feature. The α value is an eighth parameter for vectors (after the coordinates and RGB intensity) or a fifth value for voxels (with implied coordinates) specifying blending properties for the intensities of that object. Visibility of an incoming voxel or data object can thus be made dependent on object opacity or transparency and therefore depth (z_v) in the rotated view (see below). Earlier we discussed ways in which the geometric transformation could be modified to encode additional z-information into the display geometry. In addition to z-related blending operations, the compositing algorithm can retain z-information within the displayed intensities using alternative algorithms.

How Can Intensities Be Used to Retain *z*-Information

z-Coordinate or Height Views

The **height**, **range**, **topological**, **relief** or (the author's preference) ***z*-coordinat**e view (e.g., Boyde, 1987; Freire and Boyde, 1990; Forsgren *et al*., 1990; Odgaard *et al*., 1990) technique has been used for many years to directly record the z_v-depth in the intensity or color space (or both) of the display. The rule includes a test that selects a particular voxel along the observer's line of sight. The z_v-coordinate is then assigned [after an offset (z_o) and scaling (z_f)] to a value in the view. A range of z-coordinate tests, similar to the intensity tests (Eqs. 19, 20) above, are found (Fig. 14.15):

- **Coordinate of Maximum Intensity**

$$\text{if } [\, I(x_v, y_v, z_v)_n \geq V(x_v, y_v, z_v)_{n-1}] \text{ then } \quad V(x_v, y_v)_n = z_o + z_f z_{v,n} \tag{24}$$

- **Coordinate of First Intensity ≥ (t)** (i.e., **Maximum Height** or **Nearest**)

$$\text{if } \{[I(x_v, y_v, z_v)_{n-1} > t] \;\&\; [(z_{v,n-1}) < (z_{v,n})]\} \text{ then } V(x_v, y_v)_n = \text{etc.} \tag{25}$$

These z-coordinate modes are used by simple 3D topology programs (e.g., Automontage) as well as some renderers including Analyze, VolumeJ, Lasersharp. etc.

- **Iso-Intensity Surface**

$$\text{if } [I(x_v, y_v, z_v)_{n-1} = t)] \text{ then } \qquad (\text{etc.}) \tag{26}$$

Although related to the previous projections, the iso-surface routine is usually implemented by a recursive 3D algorithm such as the marching cubes (Lorensen and Cline, 1987) and is the basis of many surface object segmentation algorithms (e.g., Voxblast and Analyze).

Through-focus images from widefield microscopy have been processed using a maximum test applied to a prefiltered version of each frame. For example, the maximum local variance can produce an auto-focus intensity or coordinate view (c.f., Automontage). The depth discrimination of the confocal microscope allows a simpler auto-focus routine using just maximum brightness (for a single-surface object). This requires that the z-response for the particular specimen (point, plane, etc.) has no significant side lobes (the confocal PSF is investigated by Shaw and Rawlins, 1991). Instead of replacing the brightness with z_v, intensities can be modified (weighted) by their z-coordinate giving a so-called depth-weighted projection (Fig. 14.16). The simplest form is a linear weighting from 1 (nearest the observer) to 0 (furthest away).

- **Linear Depth-Weighted Projection**

$$V(x_v, y_v) = C[I(x_v, y_v, z_v)z] \tag{27}$$

where $z = (z_{\text{back}} - z_{v,n})/(z_{\text{back}} - z_{\text{front}})$, that is, a normalized z-coordinate. A more sophisticated form is

- **Exponential Depth Weighting**

$$V(x_v, y_v) = C[I(x_v, y_v, z_v) *f^z] \tag{28}$$

where f is a constant ≤1.

This algorithm (which can be implemented in any z-order) is often described as an attempt to model the absorption of light from a source directed along the z-axis of the data from behind (transmitted) or the attenuation of emitted fluorescence. Not surprisingly it turns out that this result is identical to that achieved by an ordered recursive algorithm traversing the data from front to back using a constant α-blending factor (≤1):

- **Recursive Exponential Weighting**

$$V(x_v, y_v) = C\{[(1 - f)^* \, I(x_v, y_v, z_v)_n], [I(x_v, y_v, z_v)_{n+1}f]\} \tag{29}$$

The commonest form of Eqs. 27 to 29 is a linear average or summation, but any compositing function can, in principle, have a depth-weighted component. By making the factor equal to

$$f = z_{\text{str}}/(Nn), \tag{30}$$

where N is the number of serial planes in the projection, a non-linear projection of strength equal to z_{str} is obtained. If $z_{\text{str}} = N$, the result is identical to a Kalman average. For $z_{\text{str}} = 1$, the front or maximum height voxels completely dominate the view. Other values give intermediate results [Fig. 14.16(A–C)].

Hidden-Object Removal

Z-Buffering

z-Ordered compositing simplifies the implementation of *z*-algorithms. Front-to-back projections using the first-object test

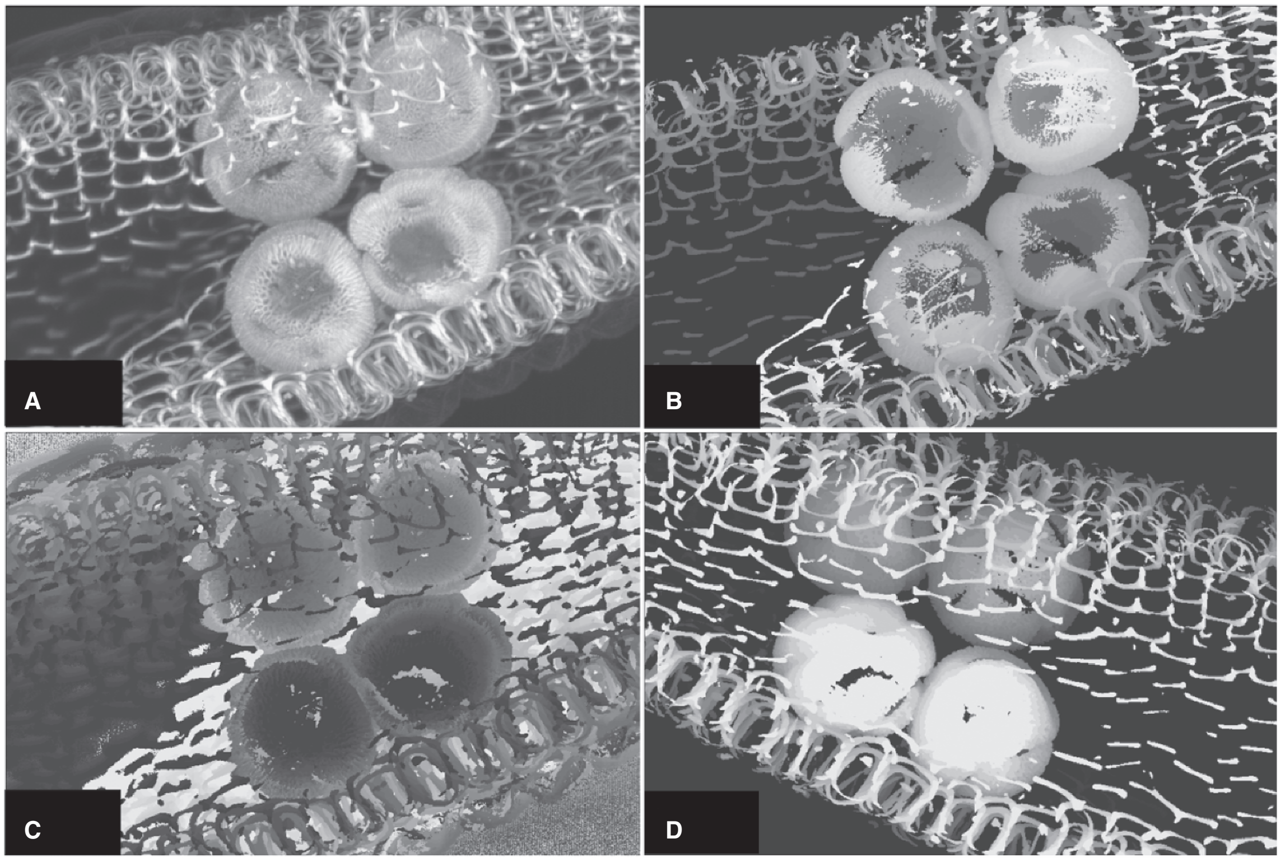

FIGURE 14.15. ***Z*-coordinate views.** (A) Maximum intensity projection of serial confocal optical sections through pollen grains in a partially dissected plant anther. Some sections are missing from the data stack (or perhaps the specimen is incomplete) but it cannot be elucidated whether the loss is from the top or bottom of the set from this projection, which carries no *z*-information. (B) shows a height or distance projection where the brightness is coded by axial distance from the viewer (dark is furthest away) recording the first voxel above a background threshold. It can now be seen that the lost sections are at the top of the stack which was projected top-to-bottom. (C) shows the height of each voxel chosen by maximum projection in (A), confirming the finding from (B). (D) shows the same algorithm as in (B) projecting bottom-to-top through the stack.

merely check if a non-zero intensity has been encountered. Hidden voxels are never processed. Conversely, if a back-to-front pass is used, the last voxel will be the one displayed and no test is required. The entire volume is now traversed and all voxels are processed. This can be very informative if the rendering process is visible on an interactive display. For non–*z*-ordered objects, a more intensive logical comparison of intensities and/or *z*-coordinates is needed, such as a front-object *z*-test; this is known as ***z*-buffering** and is a fundamentally important OpenGL-controlled process in modern graphics systems. Implementation can be at various stages of the rendering process. Voxel data is *z*-buffered efficiently as a whole section operation after warping. Polygon-ordered rendering uses standard pixel *z*-buffering but does not use information about adjacent vertices efficiently. Scan line *z*-buffering is more economical. It is intimately associated with the scan conversion of polygon edges to pixels line-by-line without needing a full 2D *z*-buffer. Spanning scan line *z*-buffering is highly optimized to extract visible object(s) from all structures that intersect the screen line that is currently being drawn. Modern graphics hardware can encompass intensity, *z*-buffer, and α-planes to program all of the computations described above into the display logic, releasing the processor for other computations.

Local Projections

The compositing functions described above can be used in combination for more control over the rendered objects. A conflict exists between hidden-object removal and significantly modifying the image intensities (by excessive use of α factors and lighting terms). A novel solution is implemented in the Lasersharp visualization program: the trick is to use coordinate or *z*-buffer algorithms to derive a segmentation reference (R_z) for projected pixels in the final view. R_z defines the *z*-coordinate of a surface [e.g., by maximum intensity (Eq. 24)] or boundary [e.g., by maximum height above threshold (Eq. 25)], etc. R_z (for each view pixel) can then become the center for a *z*-banded or **local projection**. This technique is another example of an intelligent *z*-buffer. The range of the local projection is defined by z_{front} and z_{back} given as *z*-offsets from the reference. Useful local projections include:

(1) **Reference Height Above Threshold + Local Maximum Intensity**, e.g., **Maximum Height ≥ t (Reference)**.

if $\{[I(x_v, y_v, z_v)_{n-1} > t] \; \& \; [(z_{n-1}) < (z_n)]\}$ then $R_z(x_v, y_v) = z_n$

followed by

Local maximum intensity

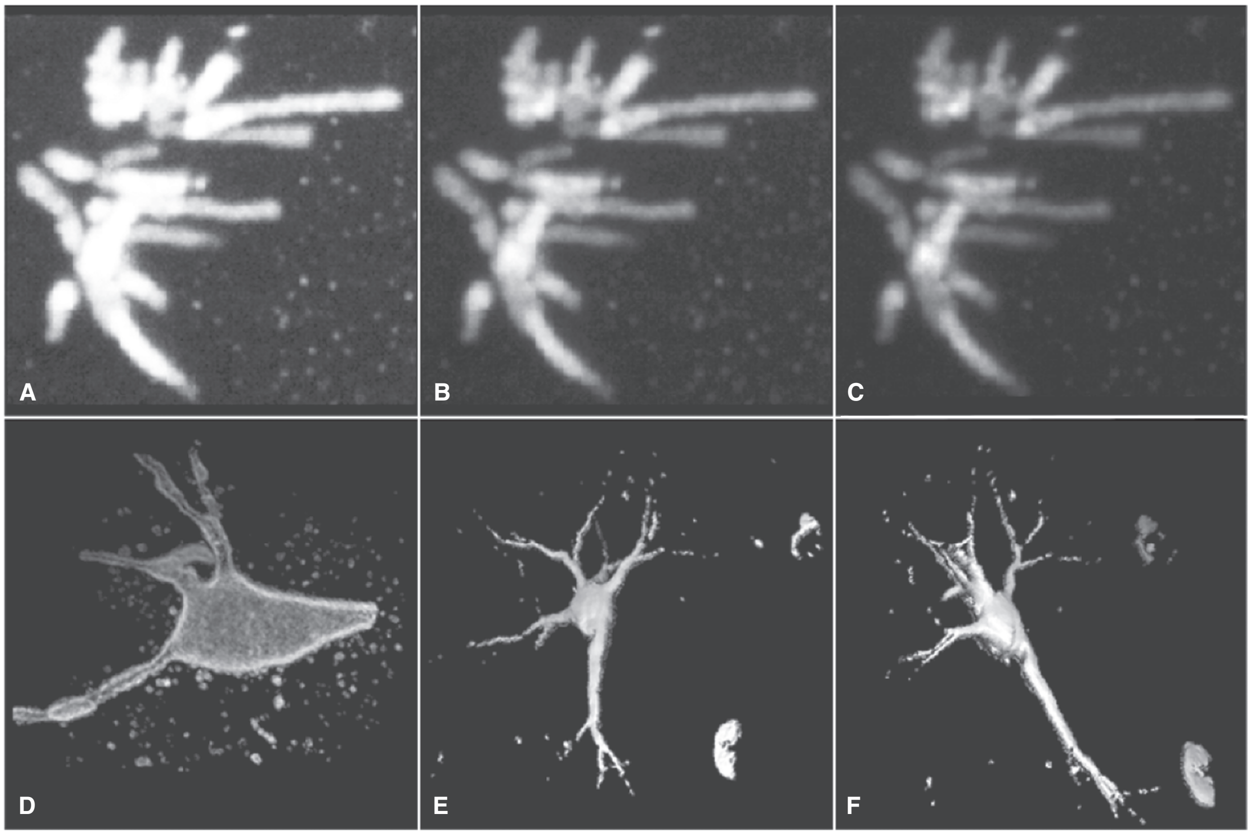

FIGURE 14.16. Depth weighting. (A–C) MPL "non-linear average" depth-weighted projections (see text) with "strengths" of 1 (A), 3 (B) and 9 (C) (number of sections = 50). MicroVoxel "depth-weighted" views (D) summation (average), (E,F) "first mode" renderings of nerve cells.

if $[\mathrm{I}(x_\mathrm{v}, y_\mathrm{v}, z_\mathrm{r}) \geq \mathrm{V}(x_\mathrm{v}, y_\mathrm{v}, z_{\mathrm{r}-1})]$ then $\mathrm{V}(x_\mathrm{v}, y_\mathrm{v}) = \mathrm{I}(x_\mathrm{v}, y_\mathrm{v}, z_\mathrm{r})$

where $[\mathrm{R}_z(x_\mathrm{v}, y_\mathrm{v}) + z_\mathrm{front}] \geq z_\mathrm{r} \leq [\mathrm{R}_z(x_\mathrm{v}, y_\mathrm{v}) + z_\mathrm{back}]$, (i.e., the local range).

Similarly one might use

(2) **Height at Maximum Intensity + Local Kalman Average.**

(3) **Height at First Intensity $\geq \mathbf{t_1}$ + Offset Local Height at Intensity $\geq \mathbf{t_2}$**

e.g., with $z_\mathrm{front} < z_\mathrm{back} < \mathrm{R}_z(x_\mathrm{v}, y_\mathrm{v})$.

(4) **Height at Maximum Intensity + Offset Local Maximum Intensity**

e.g., with $z_\mathrm{back} > z_\mathrm{front} > \mathrm{R}_z(x_\mathrm{v}, y_\mathrm{v})$.

Local projections 3 and 4 use a range that is offset from, that is, does not span, R_z. This is an objective way to segment a second object or surface within a given range of a more dominant primary feature (which is used for the reference). Thus, a plant cell wall or animal cell membrane may be found by a reference segmentation, and then structures within z_front voxels outside or z_back voxels inside the cell can then be projected in isolation. Comparative results of some local projections from Lasersharp are shown in Figure 14.17.

Adding Realism to the View

The algorithms discussed so far use test and compositing rules to project multi-dimensional images into the view space. Views of macroscopic objects contain depth cues (similar to those described above) along with textural cues arising from the position and properties of light sources. These can be used to add realism to reconstructed views in microscopy by (1) mimicking artificial macroscopic lighting effects or (2) developing a more objective visualization model incorporating *a priori* knowledge concerning the optical properties of the sample. Advanced algorithm options are listed in Table 14.9 and described in Figures 14.18, 14.19, 14.21, and 14.22 with example results in Figures 14.17 and 14.20.

Artificial Lighting: Reflection Models

The ambient lighting of the model assumed above has no directional components. Artificial lights have intensity (photometric), directionality (geometric), and color (chromatic) properties. These characteristics interact with the material properties of data objects to modulate the rendering process. Local lights are near or within the data volume and infinity sources are parallel rays coming from infinity. Ambient lighting is a general level diffused by multiple reflections off all objects within the volume, as distinct from light coming direct from the source to a given object. Reflections from

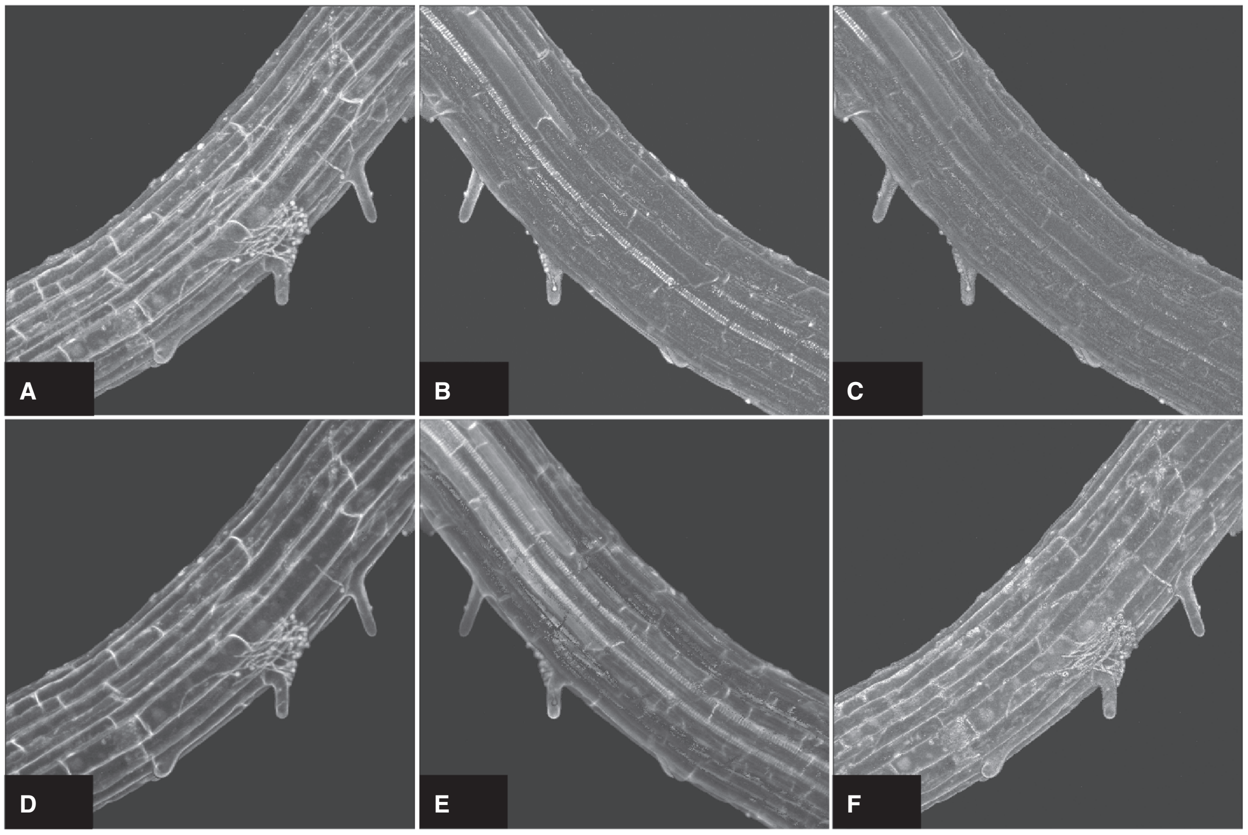

FIGURE 14.17. Local projections. These 3D views are made from the same data set shown in Figure 14.14. (A,B) show local projections where the maximum intensity is found through about one third of the depth of the sample above and below each voxel found by a previous application of the "above threshold" rule. (A) is from above and (B) below. (C,F) show the same operations applied through a depth of about one tenth of the sample thickness from the reference voxel. More structures towards the outer surface of the root are apparent compared to regular maximum projections, masking underlying features. (D,E) are local average projections corresponding to (A,B). Normalizing these intensities to fit the dynamic range of the display leads to lower contrast views than in (A,B) but shows some weak thiol-staining more clearly against the vascular autofluorescence. These views are more amenable to direct quantification than *z* or b.

an object (Fig. 14.18) can be approximated by a function (L) composed of (1) ambient reflections (L_a), (2) diffuse reflections (L_d), and (3) specular highlights (L_s) (strongest in the source direction).

$$L = L_a + (L_d + L_s)/(z_{obj} + \text{constant}) \quad \textbf{(31)}$$

where z_{obj} is the distance (in z_v of the object from the observer).

The denominator in Eq. 19 is an approximation to the z_v^2 denominator from the diffuse reflection law of Lambert (Born and Wolf, 1991, p. 183) for cases where z_{obs} is large compared to the object size. Each component L_m is the product of the light source intensity S_m, reflectivity R_m (a material property), and a direction term D_m (m = a, d, or s). The color of a voxel is determined by the

TABLE 14.9. Overview of "Realistic" Visualization Techniques for Multi-Dimensional Biological Microscopy Data

Feature	Parameter	Minimum Required	Desirable additional enhancements
[a]Visualization models		Voxel render	Shaded surface, Voxel gradient. Lighting models, SFP, Embedded objects
Material properties	color	RGB channels	Arbitrary colors/channels
	opacity		α-channel, channel dependent
	reflection		Diffuse, Specular ("shiny"), Interactive control
			Hardware texture mapping
	emission	Simulated fluor.	
	Hidden-objects	Software *z*-buffer	Hardware *z*-buffer
Surface shading models			Flat, Incremental, Gourard, Phong model
Artificial lighting	Color	RGB	Arbitrary colors & sources
	Lightable objects	Voxels	Voxels, Surface normal
	Lighting models	Ambient/diffuse	Voxel gradient, Smoothed voxel "surface,"
		(brightness)	Phong surface normal, Fast mode, Precision mode

[a]Realistic visualization modes are often used to promote particular packages, and **often with carefully chosen data!** Control of the object material properties and a clear understanding of each parameter are essential. The final reconstructed view should always be studied along with a record of all the steps and variables and preferably alongside the original image sections.
[b]Material properties and artificial lighting should be standardized for each view if intensity information is to be reliably compared between results (particularly for SFP and gradient-lit voxel modes). Hardware acceleration has made possible more interactive 3D views and "real-time" processing of modest data sets on desktop PCs.

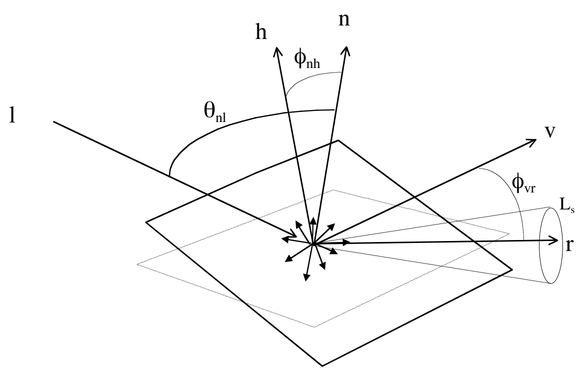

FIGURE 14.18. The artificial lighting model. Ambient lighting contributes only to the overall image brightness and has no directional components. An artificial light source is directed along l with parallel rays. Diffuse reflections from the object surface (solid panel) emanate in all directions (L_d). Some of L_d may be seen by the viewer along v. Specular reflections (L_s) occur in a narrow cone around the "reflection" direction r (θ_{nl} away from the surface normal n). These are observed along v if ϕ_{vr} is small enough. The width of the cone depends on the shininess term (see text). The Phong model describes this geometry in terms of ϕ_{vr} and θ_{nl}. Blinn showed that only ϕ_{nh} (between the surface normal and a theoretical plane, shaded, that would reflect all light from l to v) was needed for parallel lighting and a stationary observer.

light emanating from it. In general, colors are differentially reflected, absorbed, and fluorescently emitted (see below). The reflection components (Fig. 14.18) are

$$L_a = S_a R_a D_a \quad \textbf{(32)}$$

where S_a is the ambient light level (constant), R_a is the diffuse reflectivity, and D_a equals 1.

$$L_d = S_d R_d D_d \quad \textbf{(33)}$$

where S_d is the source intensity, R_d is the diffuse reflectivity, and D_d is $\cos\theta_{nl}$

$$L_s = S_s R_s D_s \quad \textbf{(34)}$$

where S_s is the source intensity, R_s is the specular reflectivity, and D_s is $\cos^{sh}\varphi_{vr}$

where θ_{nl} is the angle between the local object surface normal and the light source direction; φ_{vr} is the angle between the reflection angle (center of the highlight) and the viewing angle; and sh is the shininess parameter, which for a perfect mirror is infinite.

This full form is the Phong model (Phong, 1975) and ignores secondary reflections (i.e., is a local approximation).

A global version requires multiple rays to be followed through many reflections. This is known as ray-tracing (as distinct from ray-casting often used for voxel projection methods) or photorealistic rendering (Kriete and Pepping, 1992) and is very computationally intensive. Ray-tracing applies reflection rules to rays from the source as they bounce from surface to surface within the volume. In practice, tracing is limited to rays seen by the viewer and the depth or number of surfaces considered is also restricted. The best implementations use an adaptive depth method varied according to local material properties (Watt, 1989). In the Phong model, as the shininess factor increases, the highlight sharpens and can be seen through a smaller angle (φ_{vr}) around the reflection angle ($2^*\theta_{nl}$ away from the light source, i.e., on the other side of the surface normal). The Phong model is thus a simple, local approximation in terms of the light source direction, surface normal, material properties, and the viewing angle.

The computation can be simplified. For a light source at infinity, the viewing and lighting angles are constant over the volume. φ can then be expressed as the angle (φ_{nh}) between the surface normal (n) and the normal to a hypothetical surface (h) that would reflect all light to the viewer (Blinn, 1977). Then $\varphi_{nh} = \varphi_{vr}/2$ so larger values of sh are needed. These approximations mean that only the surface normal changes during rotations. A fast-lighting look-up table (L-LUT) can be used to precalculate the reflection terms and the surface normal used to index the L-LUT. Moving lights are also easy to implement because a static view has constant surface normals. Finally, the Phong model gives rise to (1) diffuse reflections that are the same color as the material, (2) specular highlights the same color as the light source, and (3) if the (z_{obj} + constant) term is ignored, flat surfaces (e.g., facets of a polygonal net) exhibit no shading variations. The RGB version of the Phong/Blinn model uses separate coefficients for each primary color

$$L(r,g,b) = S_a R_a (r,g,b) + S_d (R_d (r,g,b) \cos\theta_{nl} + R_s \cos^{sh}\varphi_{nh}) / (z_{obj} + \text{constant})_{\text{optional}} \quad \textbf{(35)}$$

This is the usual tri-color space model. More subtle effects are obtained by using more than three channels. Imaris is a good example of a package with flexible lighting and materials properties options that include ambient, diffuse, and specular reflection colors and light emission characteristics (see also discussion of absorption and emission below).

Enhancing the Phong and Blinn Models

Criticisms of the basic reflection scheme include rather flat surfaces and an artifact at the polygon edges where the intensity changes rapidly. The eye overreacts because it is so well adapted to detect edges by the brightness second derivative. A thin bright Mach band is seen (Watt, 1989) and the rendered view has a synthetic appearance. Incremental surface shading is then required (Figs. 14.19, 14.20). Techniques are available to minimize these and similar artifacts, seen as stripes on many reconstructions (Amira uses surface smoothing and simplification, Cedara uses intelligent opacity to reduce Mach bands).

Gourard Shading

Incremental shading gives flat surfaces variable intensities by interpolation between the material properties at the vertices. Gourard shading (Gourard, 1971) applies bilinear in-plane interpolation between the (lit) vertex intensities. This gives a gradual change across each facet with a reduction, but not elimination, of Mach bands. Often only diffuse reflections are used because highlights not seen at the vertices cannot be reconstructed in the facet. Diffuse reflection is found in Eq. 33 for each vertex. The average surface normal for facets sharing each vertex is used to get θ_{nl}. Local vertex intensities are derived from Eq. 35. Line-by-line bilinear interpolation is then used (during the scan conversion) to vary intensity over the polygon. Gourard shading thus gives some smoothing, but with (1) residual Mach banding, (2) some artifactual loss of fine relief, and (3) discontinuities between animations of rotation sequences. Surface-shaded views are shown in Figure 14.20.

Phong Shading

Instead of using vertex intensities, Phong introduced the bilinear interpolation of vertex normals (Phong and Crow, 1975). Intensities are generated incrementally as before, but now include a spec-

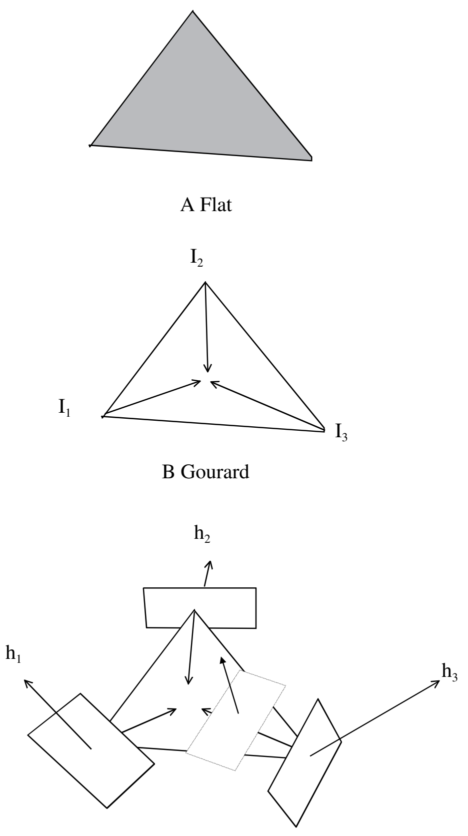

FIGURE 14.19. Incremental surface shading models. Once segmented from the voxel array, geometric objects (constructed from polygons) must be rendered to a "smooth" surface. Incremental shading is used to "fill in" the polygon areas. Flat shading (A) applies a single value (intensity, color, etc.) to the whole facet. This gives very matte views with Mach banding (see text) between facets. Gourard shading (B) interpolates the average intensity and color values (I_n) at the apices across the facet. This appears to "smooth" the surface, but still gives bands, disjointed rotations and inaccurate specular highlights. Phong shading (C) interpolates the surface normal (h_n) between the average values at each vertex across the facet. This can introduce highlights in the facet center as well as appearing to "round off" the abrupt edges and restoring the impression of a smoothly curved surface.

ular term at each point (instead of the optional Gourard single term for the whole facet). Thus, highlights within each face can now be generated, even if none was apparent at any vertex. Light sources are still at infinity so only the surface normal varies, but now within each facet. Thus, Phong interpolation tends to restore the curvature lost when a polygonal surface is approximated during segmentation or iso-surface coding. Phong interpolation can be speeded up with Gourard-type averaging in subregions of each face. A better efficiency return is to be gained by using the H-test (Watt, 1989) that decides which facets require a highlight and thus Phong shading. The rest are Gourard shaded with no quality loss. All packages that render graphical objects use surface shading with lighting and, perhaps, material properties. The user should carefully determine which modes are being used for any given rendering in order to correctly interpret the sophisticated views obtained.

Advanced Reflection Models

Although the Phong model attempts to mimic diffuse reflection by Lambert's law, the $\cos^{sh}\Phi$ specular terms are still empirically derived. Cook and Torrance (1982) modeled reflections, with advanced specular terms, using a physical model of incident light energy. The specular term is derived for micro facets within a locally averaged surface. Detailed surface models were also developed by Blinn (1977) and Torrance and Sparrow (1967). Cook and Torrance resolved the specular term into wavelength-dependent components using material refraction and the Fresnel equations (see Born and Wolf, 1991), thus modeling dispersion. Local and extended light sources have been simulated by Warn (1983) and others. Such advances produce smaller and smaller returns for the microscopist seeking to objectively render confocal images. The computational expense of even more sophisticated reflection models is rarely justified because the fine-tuning of relevant material properties cannot be reliably accomplished for biological specimens.

Gradient Lighting Models for Voxel Objects

A surface normal is used for all reflective lighting models. Local topology must, therefore, be accurately determined. For rastered voxel data, the computations are greater in number and more prone to noise, etc. Fluorescence CLSM images suffer particularly from low signal-to-noise ratio (Sheppard *et al.*, 1992) and must therefore always be carefully filtered and/or PSF-deconvolved before gradient segmentation or lighting algorithms are applied. Gradient filters for edge and surface segmentation (Eq. 15) are often also used to highlight boundaries for voxel gradient lighting models (Fig. 14.20; see also Forsgren *et al.*, 1990; Odgaard, 1990). An alternative to these expensive 3D filters is to use a height or *zx*-coordinate view $z_{co}(x_v, y_v, z_v)$ (Eqs. 24–26). Surface normals can be derived from a local gradient in z_{co} in 2D V space (Gordon and Reynolds, 1985; Aslund *et al.*, 1988). This is the basis for post-lighting models (Fig. 14.21), which apply the lighting algorithm to a 2D *z*-buffer after the data projection stage (c.f., VoxBlast).

$$\mathrm{grad}(x_v, y_v) = |\,[(dz_{co}/dx_v)^2 + (dz_{co}/dy_v)^2 + 1] =$$
$$|\,\{[z_{co}(x_v + 1) - z_{co}(x_{v\,-}\,1)]^2 + [z_{co}(y_v + 1) - z_{co}(y_{v\,-\,1})]^2\,\}\,/\,2 \qquad \mathbf{(36)}$$

The quantization of depth in z_{co} can give rise to artifactual edge effects, so at least 10- and preferably 16-bits of *z*-buffer are desirable. In both this and the 3D filters, steep gradients cannot be distinguished easily from discontinuities.

Artificial Lighting: Absorption and Transparency

Transparency can be modeled by an attenuation coefficient applied to each object. This can: (1) modify the light emanating towards the viewer (emission), (2) attenuate artificial light as it passes from the source through the data volume (illumination or excitation), and (3) modify the light emanating from an object that contributes to the lighting of another. Ray-tracing is required to properly implement (3). The first process (1) is the most often encountered in visualization programs. All objects are evenly lit by the ambient light, which does not include attenuation by nearby objects. Each object brightness is seen by the observer according to its opacity/transparency. This is achieved by α-blending (Eq. 22) with an α value derived by using the object intensity as an index into an opacity/transparency look-up table (OT-LUTs). By using the back-to-front projection, the combined opacity of all other objects through which the imaginary rays pass is taken into account.

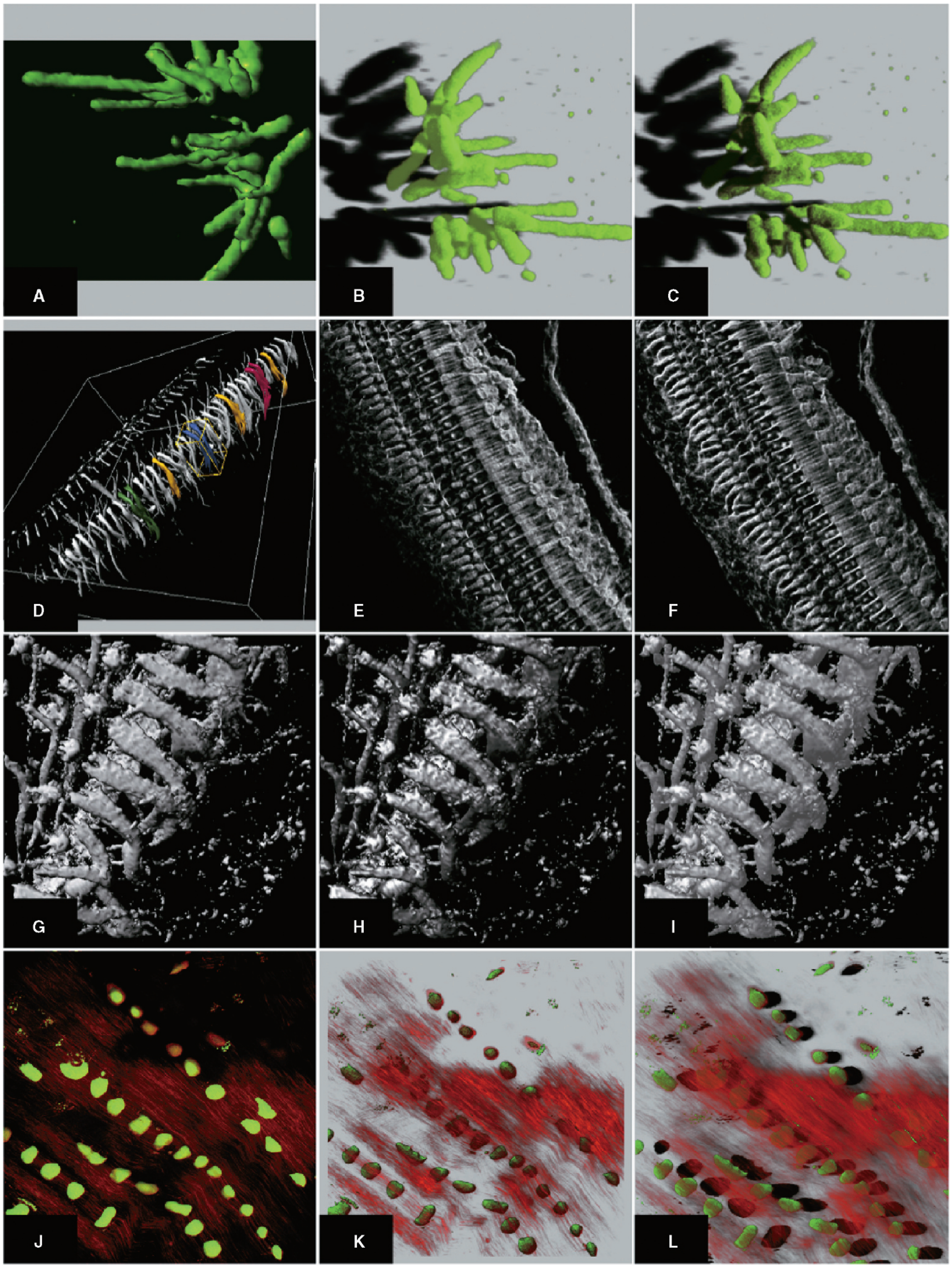
A
B
C
D
E
F
G
H
I
J
K
L

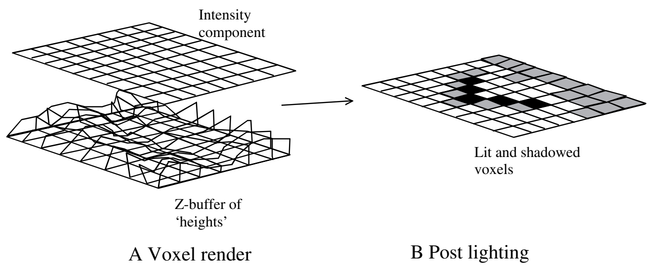

FIGURE 14.21. Post lighting is a rapid way of interactively applying lighting models to pre-rendered views. The z_v information is retained during the voxel intensity render in the z-buffer as a "height" view (A). If an iso-intensity surface is defined or a constant segmentation threshold used the intensity view may show little or no detail [upper part of (A)]. Local relief in the z-buffer is interrogated to produce a map of surface normals that are used as pointers into a fast lighting L-LUT (see text). These lighting terms are used to highlight and shadow the rendered voxels (B).

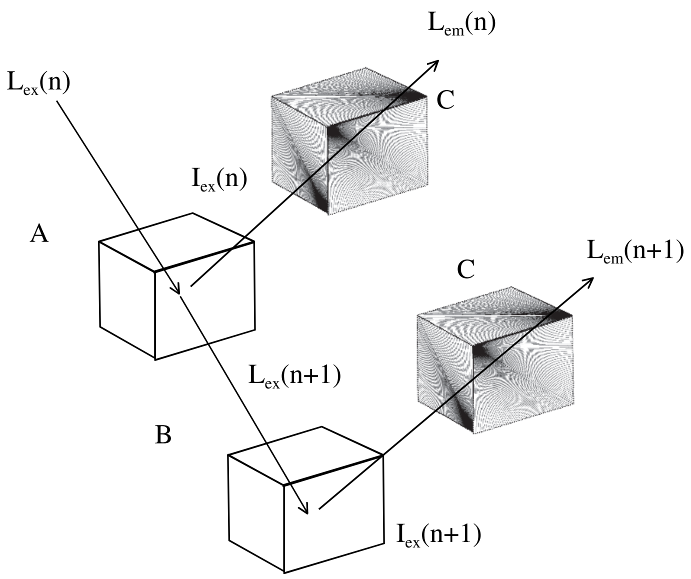

FIGURE 14.22. The simulated fluorescence process (SFP) algorithm (see also Fig. 14.20) attempts to simulate the excitation and emission from fluorescent features. Excitation light L_{ex} excites voxels in successive planes (n, n+1, etc.). Each illuminated voxel (I_{ex}) emits fluorescence (L_{em}) in all directions. Some of L_{em} is seen by the viewer. Excitation light not absorbed by the voxels in plane n (A) excites regions in plane n+1 (B), etc. Similarly, emitted light from each plane passes through other voxels (C) as it travels out of the volume. Absorption of L_{em} thus follows, but re-excitation by L_{em} is usually ignored. Separate absorption co-efficients for L_{ex} and L_{em} are used for selective control of transparency (see text).

Opaque objects at the front of the volume hide those at the back. The OT-LUT may have separate partitions for different structures within a single volume. Kay and Greenberg (1979) used the z_v component of the surface normal to attenuate rays traversing polygons. For voxel objects, the average opacity at each voxel is sufficient. This basic attenuation produces no lateral shading or shadowing.

The excitation part of the model (Eq. 2) is used to simulate the attenuation of illumination between a source at infinity and data objects. An excitation source is positioned at infinity with direction $L = (L_x, L_y, 1)$. This light illuminates the rotated image $I(x_v, y_v, z_v)$ by a plane wavefront normal to L passing through the volume. This wavefront intersects with the volume in serial (oblique) planes. Voxels cut by the nth plane during the excitation phase are given by

$$I(x_{ex}, y_{ex}, n) = I(x_v + L_x n, y_v + L_y n, n) \qquad \textbf{(37)}$$

The components of the lighting vector can be made integers to speed up computations. As the excitation wave propagates through the volume, it is attenuated by preceding layers of objects according to an excitation extinction coefficient α_{ex}. Usually the object (or voxel, etc.) intensity is used to represent the amount of absorbing material at each position (α can be varied by an OT-LUT). The excitation wavefront at the nth plane is now

$$L_{ex}(x_{ex}, y_{ex}, n) = L_{ex}(x_{ex}, y_{ex}, n-1)(1-\alpha_{ex})\, I(x_{ex}, y_{ex}, n) \qquad \textbf{(38)}$$

A lit or excited image volume I_{ex} can then be constructed

$$I_{ex}(x_{ex}, y_{ex}, n) = I(x_{ex}, y_{ex}, n)\, L_{ex}(x_{ex}, y_{ex}, n) \qquad \textbf{(39)}$$

This illuminated volume could be plugged directly into the reflection model. Alternatively, one can simulate the light emitted by each object as if it was self-luminous or fluorescent (Fig. 14.22). The simulated fluorescence process (SFP) has been refined by a number of workers (e.g., van der Voort *et al.*, 1989; Brakenhoff *et al.*, 1990; Hallgren and Buchholz, 1992; Messerli *et al.*, 1993). Excitation and emission phases are implemented as before. The

FIGURE 14.20. "Realistic" views by surface shading, gradient voxel and other lighting effects. (A) shows a Gourard-shaded geometric object surface rendering of one set of chromosomes from the plant *Milium* (Bennet *et al.*, 1990), using the Geometry render module of the AVS package. (See also Levoy 1988; Rigaut *et al.*, 1992, for Gourard-shaded reconstructions using the Visilog software). Since the segmented geometric polygons are very numerous but small, Mach band effects (see text) and the corruption of reflection highlights are not obvious, though the views have a certain "plastic" or "synthetic" look. (B–J, and L) are produced by the Imaris software. (B,C) show the same confocal data as (A) visualized using a simulated fluorescence process (SFP) voxel-based algorithm. Directional lighting (and resultant shadows) can be controlled independently from the ambient lighting (similar to a fluorescence emission property) to achieve stronger shadows (C) or a more "luminous" fluorescence (B). (D) shows the use of segmented objects and artificial colors to highlight individual or pairs of hair cells in this reconstruction of confocal data (courtesy of Bio-Rad Microscience) from a mouse inner ear preparation. (E, F) show voxel gradient lighting applied from the left and right respectively to a top-down reconstruction of the same data as (D). Combining object segmentation, surface shading and a Phong lighting model allows a material property defining reflectance to be attributed to structures. (G) shows a selected portion of the inner ear data surface rendered with a diffuse lighting model only. (H) shows a specular (highlight) lighting model and (J) combines the specular model with an ambient model rather like the SFP algorithms. (J) shows a two-channel fluorescence data set obtained by multi-photon LSM through rat intervertebral disk tissue (in consultation with Dr. R.J. Errington, Cardiff University, UK) and shows CMFDA-stained chondrocytes and autofluorescent extracellular matrix (mostly collagen) (Metamorph software). (K) shows the same data by a combination of surface-shaded object rendering (of the cells) and voxel-based rendering (of the ECM) with some directional lighting and careful application of transparency to render the tissue transparent. (L) shows the same data visualized by the SFP algorithm, exhibiting the characteristic shadows that are an optional feature of this method.

emitted light propagates to the viewer in a direction described by the vector (v) where

$$\mathrm{v} = (\mathrm{v}_x, \mathrm{v}_y, 1) \tag{40}$$

The emitted light wavefront L_{em} is then found by:

$$\mathrm{L}_{\mathrm{em}}(x_{\mathrm{v}}, y_{\mathrm{v}}, n-1) = \mathrm{I}_{\mathrm{em}}(x_{\mathrm{v}}, y_{\mathrm{v}}, n-1) + \mathrm{L}_{\mathrm{em}}(x_{\mathrm{v}}, y_{\mathrm{v}}, n) \\ [1 - \alpha_{\mathrm{em}}) \, \mathrm{I}(x_{\mathrm{v}}, y_{\mathrm{v}}, n-1)\} \tag{41}$$

where $\mathrm{I}_{\mathrm{em}}(x_{\mathrm{v}}, y_{\mathrm{v}}, n) = \mathrm{I}_{\mathrm{ex}}(x_{\mathrm{v}}, y_{\mathrm{v}}, n)\, A(x_{\mathrm{v}}, y_{\mathrm{v}}, n)$.

A is an empirical term encompassing the quantum efficiency and emissivity of the object. (This may be set to unity, i.e., determined solely by α_{ex}.) α_{em} is the opacity (or OT-LUT) for the emission wavelength. The emission computation is carried out in the reverse *n* order compared to excitation. A consequence of this absorption/emission model is the casting of shadows by the two waves as they pass densely absorbing structures. These shadows may fall onto the background or onto underlying structures. Coefficients should be implemented separately for each channel of a multichannel image. Opacity in one channel can then be used to modulate intensities in another, as in the Imaris and LCS (Leica) SFP mode. AVS uses a two-pass transparency operator to achieve a similar result.

HOW CAN I MAKE MEASUREMENTS USING THE RECONSTRUCTED VIEWS?

Direct measurements from image data can sometimes be automated (Cohen *et al.*, 1994; see also Chapter 15, *this volume*), but interactive 3D analysis often requires feedback from the volume reconstruction. Views are used in several ways during multi-dimensional measurements (a few examples are shown in Fig. 14.23).

(1) One or more sections may be displayed as a montage and their intersection with an interactive screen cursor used to pinpoint original image voxels in 3D. The image data can then be used to obtain a 3D intensity measurement. This gives the highest spatial and photometric reliability but cannot be used for complex structures that are not discernible from a few intersecting sections. The exception to this rule involves the use of stereological estimators to probe sections randomly oriented within the volume (e.g., see Analyze volume measuring tool). This is a particularly good method of estimating complex 3D measures such as surface area (e.g., Howard and Sandau, 1992) or orientation (Mattfeldt *et al.*, 1994). Other grid-sampling estimators (e.g., Gundersen *et al.*, 1988) have been implemented. The approach works best when an interactive cursor is tracked simultaneously in at least three different orthogonal cross-sections. Through-focus animations in all three directions are also useful aids in identifying structures passing through many planes. The orthogonal section display with cross-hair cursor is a standard element of most visualization programs. Some also allow oblique (arbitrary) sections to be displayed for measurements.

(2) A reconstructed view may be displayed to identify features to be measured (with animation, etc.) before interrogating the original image data for the precise values of each voxel. The problem remains of how to determine exactly which image data voxels are represented by a particular feature in the reconstruction. This stems from the fact that the third spatial (or temporal, etc.) dimension has been significantly reduced. The precise method of coding this reduced dimensional information determines how accurately original voxels may be retrieved. The method is most successful where high contrast objects have been efficiently segmented. An elegant solution is to embed a voxel section into a 3D rendered view so as to show both the reconstruction and the original data (see Amira, Analyze, Voxblast, Imaris, Volvis, and others for examples).

(3) A third method involves the direct measurement of reconstructed views. This is possible by improving the coding method used in (2). Parallax shifts are used effectively to measure depth in stereo views (Fig. 14.24). In practice, two cursors are moved in tandem through the left and right pairs of the stereoscopic space. Tandem movements of the two cursors sweep out x_{v}, y_{v}-coordinates. Z_{v}-distances are swept out by altering the separation of the two cursor components. An observer using the appropriate stereoscopic viewing aid will perceive the cursor to track in and out of the screen. This method is particularly useful for very transparent structures. Opaque objects are measured more easily by interrogating a *z*-coordinate or surface view. The *z*-value at each (x_{v}, y_{v}) pixel allows full 3D measurements to be made of the object's surface. Reconstructions from segmented objects defined by surfaces or *z*-coordinates almost always proceed via the generation of a *z*-buffer intermediate. This can be kept in memory while an intensity reconstruction is built up on the monitor. Visible features in the intensity view (which may be artificially lit, etc.), can return their *z*-position by interrogating the *z*-buffer (this technique is used efficiently by voxel renderers such as VoxBlast). Ten- to 16-bits of *z*-buffer are desirable. Line transects through the *z*-buffer return profile plots through a structure. Area measurements in the *z*-buffer return integrated heights that are equivalent to the volume under the surface. All these measures may be made alongside equivalent x_{v}, y_{v} and intensity plots (Fig. 14.23).

Geometric objects objectively segmented from the image volume for surface visualization can also report their total surface area (and also their included volume, e.g., Guilak, 1993). Because they are defined by polygons, many statistics of shape, asymmetry, etc., can be automatically recorded. Particle analysis software is now implemented in 3D (and 4D) to count segmented objects (most object-based systems) and even track them over time (e.g., Imaris, Volocity). A more extensive discussion of computerized measurements and multi-dimensional data can be found in the following chapter.

CONCLUSION

Visualization is not a precise science, but by understanding the functions of your display program, the user can derive useful objective information from views of multi-dimensional images. Image data collected from biological microscopes is necessarily complex and noisy, and it contains ill-defined structures with largely unknown photometric and geometric statistics. Step-by-step visualization algorithms of increasing sophistication must be applied in a controlled manner, with adequate parameter tracking and validation in order to have confidence that the final results portray real features. Quantitative measurement from multi-dimensional views adds additional constraints to the artificial properties that can be added to rendered views. Simple algorithms produce the fastest visualizations. Object-based reconstruction, though supported by a vast range of affordable, yet high specification graphics hardware, is critically dependent on the segmentation used to extract the vertex geometries from original 3D voxel data. Test samples and control data should always be processed in order to understand the significance of complex rendered views. Seeing should never be used as the sole criterion for believing.

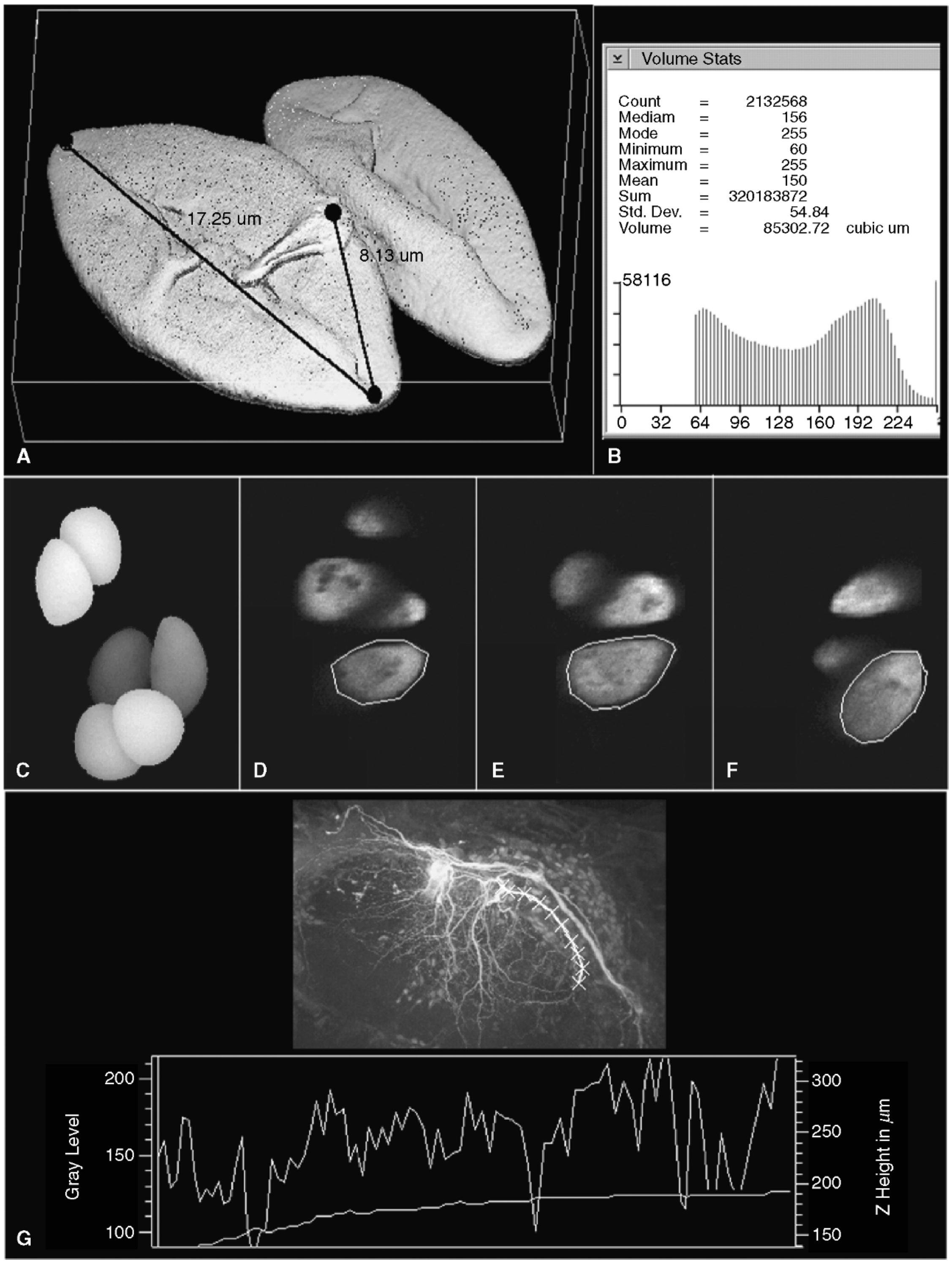

```
Volume Stats

Count     =      2132568
Mediam    =          156
Mode      =          255
Minimum   =           60
Maximum   =          255
Mean      =          150
Sum       =    320183872
Std. Dev. =         54.84
Volume    =      85302.72   cubic um
```

FIGURE 14.23. 3D Measurements on multiple sections and views. (A) shows the MicroVoxel "Caliper Tool" being used to make a distance measurement on a "First mode" rendered view of a pollen grain. (B) is a representative example of intensity statistics and 3D volume from a MicroVoxel volume measurement. (C–F) show ThruView PLUS views of living articular cartilage chondrocytes (data supplied by R.J. Errington, Physiology Dept., Oxford University) used for 3D measurements. (C) is a single time point from a 4D series of "height coded" views. Profiles and volumes of individual chondrocytes (here labeled with CMFDA) are derived directly from each reconstructed view. (D–F) show oblique sections through another data set with automatic serial "area" measurements being taken (using the MPL "area" verb in a macro program) of each segmented slice through a single cell. The corrected *z*-step applied to the integrated area sum gives a direct volume estimate. (G) shows the neurone of Figures 14.2 and 14.3, rendered using the MPL "maximum height" mode. MPL height modes automatically record both the *z*-coordinate (*z*-buffer) and the corresponding intensity view. Here the maximum intensity is shown in the inset gray-scale view with a cursor track along a prominent process. The corresponding intensity trace is shown in the upper plot and the *z*-depth in the lower trace.

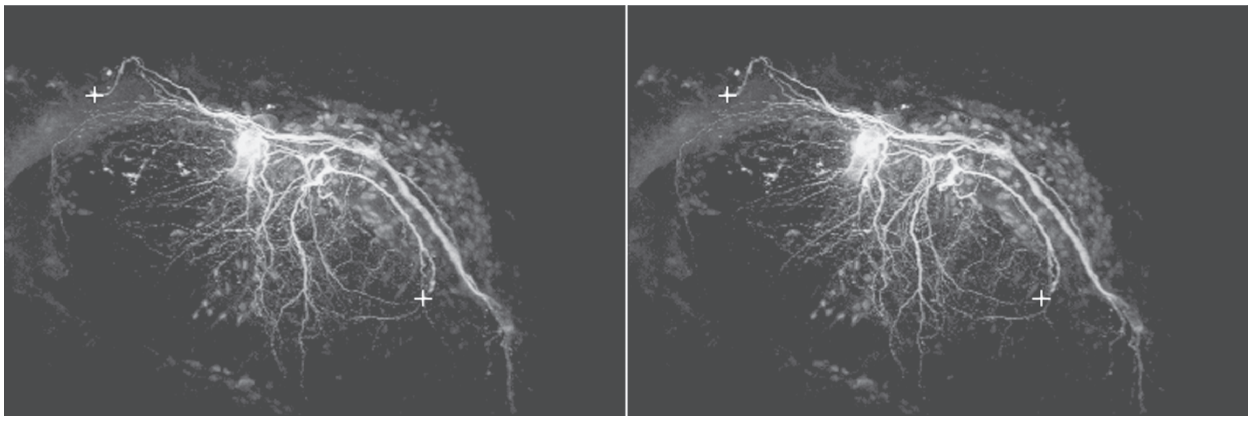

FIGURE 14.24. 3D Measurements using a stereoscopic cursor. Stereo pair of the Lucifer Yellow stained neuron also shown in Figures 14.2 and 14.3 showing the use of a pair of software-generated cursors with variable parallax shift between images to mark out *x*, *y* and *z* positions in the transparent reconstruction. These images were generated using MPL pixel-shifted maximum-intensity projections and the macro-programming language to generate the stereo cursors. On a fast '486 computer, these can be moved in and out along the *z*-direction interactively.

ACKNOWLEDGMENTS

I thank all contributors to the various sources of technical information (many of them Web accessible) for the packages listed in Table 14.1 and referred to throughout the text. Thanks also to all who provided images. The author would like to acknowledge the Wellcome Trust and the Sir William Dunn School of Pathology, University of Oxford, where he is Research Manager of the Bioimaging Service.

REFERENCES

Agard, D.A., Hiroaka, Y., Shaw, P., and Seadt, J.W., 1989, Microscopy in three dimensions, Methods Cell Biol., 30:353–377.

Aslund, N., Liljeborg, A. Forsgren, P.-O., and Wahlsten, S., 1988, 3D scanning reconstruction, *Laboratory Practice*, 37:58–61.

Bennet, S.T., Fricker, M.D., Bennet, M.D., and White, N.S., 1990, The 3D localisation of chromosomes using confocal microscopy, *Trans. Roy. Microscopic. Soc.* 1:441–444.

Blinn, J.F., 1977, Models of light reflection for computer synthesised pictures, *Computer Graphics* 11:192–198.

Bolsover, S., 1995, Using fluorescence to probe calcium signalling mechanisms. *Biochem. Soc. Trans.* 23(3):627–629. Review.

Born, M., and Wolf, E., 1991, *Principles of Optics*, Pergamon Press, Oxford.

Boyde, A., 1987, Colour coded stereo images from the tandem scanning reflected light microscope, *J. Microsc.* 146:137–145.

Boyde, A., 1992, Real time direct-view confocal light microscopy, In: *Electronic Light Microscopy* (D. Shotton, ed.), Wiley-Liss, New York, pp. 289–314.

Braddick, O.J., and Sleigh, A.C., 1983, *Physical and Biological Processing of Images*, Springer-Verlag, Berlin.

Brakenhoff, G.J., Van der Voort, H.T.M., and Oud, J.L., 1990, Three-dimensional representation in confocal microscopy, In: *Confocal Microscopy* (T. Wilson, ed.), Academic Press, London, pp. 185–197.

Carlsson, K., 1991, The influence of specimen refractive index, detector signal integration and non-uniform scan speed on the imaging properties in confocal microscopy, *J. Microsc.* 163:167–178.

Cabral, B., Cam, N., and Foran, J., 1994, Accelerated volume rendering and tomographic reconstruction using texture mapping hardware. In: *Symposium on Volume Visualization* (Kaufman and Krueger, eds.), ACM Press, New York, pp. 91–98.

Cheng, P.C., Acharya, R., Lin, T.H., Samarabandu, G., Shinozaki, D.D., Berezney, R., Meng, C., Tarng, W.H., Liou, W.S., Tan, T.C., Summers, R.G., Kuang, H., and Musial, C., 1992, 3D Image analysis and visualisation in light microscopy and X-ray micro-tomography, In: *Visualisation in Miomedical Microscopies* (A. Kriete, ed.), VCH, Weinhein, Germany.

Cohen, A.R., Roysam, B., and Turner, J.N., 1994, Automated tracing and volume measurements of neurons from 3D confocal fluorescence microscopy data, *J. Microsc.* 173:103–114.

Cook, R.L., and Torrance, K.E., 1982, A reflectance model for computer graphics, *Computer Graphics* 15:307–316.

Cookson, M.J., 1994, Three dimensional reconstruction in microscopy, *Proc. RMS* 29:3–10.

Cookson, M.J., Davies, C.J., Entwistle, A., and Whimster, W.F., 1993, The microanatomy of the alveolar duct of the human lung imaged by confocal microscopy and visualised with computer based 3D reconstruction, *Comput. Med. Imaging Graphics* 17:201–210.

Cookson, M.J., Dykes, E., Holman, J.G., and Gray, A., 1989, A microcomputer based system for generating realistic 3D shaded images reconstructed from serial section, *Eur. J. Cell Biol.* 48(Suppl 25):69–72.

Drebin, R.A., Carpenter, L., and Hanrahan, P., 1988, Volume rendering, *Computer Graphics* 22:65–74.

Elisa, A., Schmidt, F., Gattass, M., and Carvalho, P.C.P., 2000, Combined 3-D visualization of volume data and polygonal models using a shear-Warp algorithm, *Computer Graphics* 24:583–601.

Fahle, M., and de Luca, E., 1994, Spatio-temporal interpolation in depth, *Vision Res.* 34:343–348.

Forsgren, P.O., Franksson, O., and Liljeborg, A., 1990, Software and electronics for a digital 3D microscope, In: *Confocal Microscopy* (T. Wilson, ed.), Academic Press, London.

Freire, M., and Boyde, A., 1990, Study of Golgi-impregnated material using the confocal tandem scanning reflected light microscope, *J. Microsc.* 158:285–290.

Fricker, M.D., and White, N.S., 1992, Wavelength considerations in confocal microscopy of botanical specimens, *J. Microsc.* 166:29–42.

Frisby, J.P., and Pollard, S.B., 1991, Computational issues in solving the stereo correspondence problem, In: *Computational Models of Visual Processing* (M.S. Landy and J.A. Movshon, eds.), MIT Press, Cambridge, Massachusetts, pp. 331–358.

Foley, J.D., van Dam, A., Feiner, S.K., and Hughes, J.F., 1990, *Computer Graphics: Principles and Practice*, 2nd ed., Addison Wesley Publishing Co., Reading, Massachusetts.

Gordon, D., and Reynolds, A., 1995, Image shading of 3-dimensional objects, *Computer Vision Graph. Image Proc.* 29:361–376.

Gouraud, H., 1971, Continuous shading of curved surfaces, *IEEE Trans. Comput.* 20:623–629.

Guilak, F., 1993, Volume and surface area measurement of viable chondrocytes *in situ* using geometric modelling of serial confocal sections, *J. Microsc.* 173:245–256.

Gundersen, H.J.G., Bagger, P., Bendtsen, T.F., Evans, S.M., Korbo, L., Marcussen N., 1998, The new stereological tools: dissector, fractionator, nucleator, and point sampled intercepts and their use in pathological research and diagnosis. *Acta. Pathol. Microbiol. Scand.* 96:857–881.

Hallgren, R.C., and Buchholz, C., 1992, Improved solid surface rendering with the simulated fluorescence process (SFP) algorithm, *J. Microsc.* 166: rp3–rp4.

He, T.L., Hong, L., Kaufman, A., and Pfister, H., 1996, Generation of transfer functions with stochastic search techniques, *Proc. IEEE Visualization* 489:227–234.

Hell, S., Reiner, G., Cremer, C., and Stelzer, H.K., 1993, Aberrations in confocal fluorescence microscopy induced by mismatches in refractive index, *J. Microsc.* 169:391–405.

Holmes, T.J., and Liu, Y.-H., 1992, Image restoration for 2D and 3D fluorescence microscopy, In: *Visualization in Biomedical Microscopies* (A. Kriete, ed.), VCH, Weinheim, Germany, pp. 283–327.

Howard, C.V., and Sandau, K., 1992, Measuring the surface area of a cell by the method of spatial grid with a CLSM-a demonstration, *J. Microsc.* 165:183–188.

Hudson, B., and Makin, M.J., 1970, The optimum tilt angle for electron stereomicroscopy, *J. Sci. Instr. (J. Phys. Eng.)* 3:311.

Kay, D.S., and Greenberg, D., 1979, Transparency for computer synthesised objects, *Computer Graphics* 13:158–164.

Kindlmann, G., and Durkin, J., 1998, Semi automatic generation of transfer function for direct volume rendering, *Proc. IEEE* 170:78–86.

Kriete, A., and Pepping, T., 1992, Volumetric data representations in microscopy: Application to confocal and NMR-microimaging, In: *Visualization in Biomedical Microscopies* (A. Kriete, ed.), VCH, Weinheim, Germany, pp. 329–360.

Landy, M.S., and Movshom, J.A., 1991, *Computational Models of Visual Processing*, MIT Press, Cambridge, Massachusetts.

Lacroute, P., and Levoy, M., 1994, Fast volume rendering using a shear-warp factorization of the viewing, *SIGGRAPH* 1994:451–458.

Lorensen, W.E., and Cline, H.E., 1987, Marching cubes, a high resolution 3D surface construction algorithm. *Computer Graphics* 21:163–169.

Levoy, M., 1988, Display of surfaces from volume data, *IEEE Computer Graphics Appl.* 8:29–37.

Masters, B., 1992, Confocal ocular microscopy: a new paradigm for ocular visualisation, In: *Visualization in Biomedical Microscopies* (A. Kriete, ed.), VCH, Weinheim, Germany, pp. 183–203.

Mattfeldt, T., Clarke, A., and Archenhold, G., 1994, Estimation of the directional disribution of spatial fibre processes using stereology and confocal scanning laser microscopy, *J. Microsc.* 173:87–101.

Marks, J., 1997, Design galleries: A general approach to setting parameters for computer graphics and animation, *SIGGRAPH* 1997:389–400.

Messerli, J.M., van der Voort, H.T.M., Rungger-Brandle, and Perriard, J.-C., 1993, Three dimensional visualisation of multi-channel volume data: The smSFP algorithm, *Cytometry* 14:723–735.

Murch, G.M., 1984, Physiological principles for the effective use of colour, *IEEE Computer Graphics Appl.* 4:49–54.

Nakayama, 1985, Biological image motion processing: A review, *Vision Res.* 25:625–660.

Odgaard, A., Andersen, K., Melsen, F., and Gundersen, H.J., 1990, A direct method for fast three-dimensional serial reconstruction, *J. Microsc.* 159:335–342.

Oldmixon, E.H., and Carlsson, K., 1993, Methods for large data volumes from confocal scanning laser microscopy of lung, *J. Microsc.* 170:221–228.

Perry, V.H., and Cowey, A., 1985, The ganglion cell and cone distributions in the monkey's retina: Implications for central magnification factors, *Vision Res.* 25:1795–1810.

Phong, B.-T., 1975, Illumination for computer generated pictures, *Commun. ACM* 18:311–317.

Phong, B.-T., and Crow, F.C, 1975, Improved rendition of polygonal models of curved surfaces, In: *Proceedings of the 2nd USA-Japan Computer Conference*, ACM Press, New York, pp. 475–480.

Poggio, G., and Poggio, T., 1984, The analysis of stereopsis, *Ann. Rev. Neuro.* 7:379–412.

Richards, W., 1970, Stereopsis and stereoblindness, *Exp. Brain Res.* 10:380–388.

Rigaut, J.P., Carvajal-Gonzalez, S., and Vassy, J., 1992, 3D Image cytometry, In: *Visualization in Biomedical Microscopies* (A. Kriete, ed.), VCH, Weinheim, Germany, pp. 205–248.

Robb, R.A., 1990, A software system for interactive and quantitative analysis of biomedical images, In: *3D Imaging in Medicine*, NATO ASI Series, Vol. F (K.H. Hohne, H. Fuchs, and S.M. Pizer, eds.) 60:333–361.

Sakas, G., Grimm, M., and Savopoulos, A., 1995, An optimized maximum intensity projection (MIP), In: *Rendering Techniques '95* (P. Hanrahan and W. Purgathofer, eds.), Springer-Verlag, New York, pp. 51–63.

Shaw, P.J., and Rawlins, D.J., 1991, The point-spread function of a confocal microscope: Its measurement and use in deconvolution of 3-D data, *J. Microsc.* 163:151–165.

Sheppard, C.J.R., and Gu, M., 1992, The significance of 3-D transfer functions in confocal scanning microscopy, *J. Microsc.* 165:377–390.

Sheppard, C.J.R., and Gu, M., 1993, Modeling of three-dimensional fluorescence images of muscle fibres: An application of three-dimensional optical transfer function, *J. Microsc.* 169:339–345.

Sheppard, C.J.R., Gu, M., and Roy, M., 1992, Signal-to noise ratio in confocal microscopy systems, *J. Microsc.* 168:209–218.

Shotton, D.M., and White, N.S., 1989, Confocal scanning microscopy; 3-D biological imaging, *Trends Biochem. Sci.* 14:435–439.

Torrance, K.E., and Sparrow, E.M., 1967, Theory for off-specular reflection from roughened surfaces. *Opt. Soc. Am.* 57:1105–1114.

Van der Voort, H.T.M., Brakenhoff, G.J., and Baarslag, M.W., 1989, Three-dimensional visualization methods for confocal microscopy, *J. Microsc.* 153:123–132.

Van Zandt, W.L., and Argiro, V.J., 1989, A new inlook on life, *UNIX Rev.* 7:52–57.

Visser, T.D., Oud, J.L., and Brakenhoff, G.J., 1992, Refractive index and axial distance measurements in 3-D microscopy, *Optik* 90:17–19.

Visser, T.D., Groen, F.C.A., and Brakenhoff, G.J., 1991, Absorption and scatering correction in fluorescence confocal microscopy, *J. Microsc.* 163:189–200.

Wallen, P., Carlsson, K., and Mossberg, K., 1992, Confocal laser scanning microscopy as a tool for studying the 3-D morphology of nerve cells, In: *Visualization in Biomedical Microscopies* (A. Kriete, ed.), VCH, Weinheim, Germany, pp. 109–143.

Warn, D.R., 1983, Lighting controls for synthetic images, *Computer Graphics* 17:13–24.

Watt, A., 1989, *Three Dimensional Computer Graphics*, Addison Wesley, Wokingham, England.

Wilson, T., 1990, Confocal microscopy, In: *Confocal Microscopy* (T. Wilson, ed.), Academic Press, London, pp. 1–64.

Woo, M. (1992). *OpenGL Programming Guide*, Addison Wesley, Wokingham, England.